Synkinematic magmatism, heterogeneous deformation, and progressive strain localization in a strike-slip shear zone. The case of the right-lateral Karakorum fault

Emmanuelle BOUTONNET[a], P. H. LELOUP[a], N. ARNAUD[b], J.-L. PAQUETTE[c], W.J. DAVIS[d], K. HATTORI[e]

[a] LGL-TPE Laboratoire de Géologie de Lyon – Terre, Planètes, Environnement, UMR CNRS 5276, Université Claude Bernard Lyon 1 - ENS, France (emmanuelle.boutonnet@ens-lyon.fr)

[b] Géosciences Montpellier, UMR CNRS 5243, Université de Montpellier 2, France (Nicolas.Arnaud@univ-montp2.fr)

[c] Laboratoire Magma et Volcans, UMR CNRS 6524, Université Blaise Pascal, Université de Clermont-Ferrand, France (J.L.paquette@opgc.univ-bpclermont.fr)

[d] ESS/GSC-CNCB/GSC-CC/GEOCHRON, Geological Survey of Canada (Bill.Davis@NRCan-RNCan.gc.ca)

[e] Department of Earth Sciences, University of Ottawa, Canada (khattori@uOttawa.ca).

Corresponding author:

Emmanuelle Boutonnet. E-mail : emmanuelle.boutonnet@ens-lyon.fr

25

Abstract

New structural observations coupled with 15 U/Pb and 24 Ar/Ar new ages from the Karakorum shear zone (KSZ) constrain the timing and slip rate of the right-lateral Karakorum fault zone (KFZ), one of the great continental Asian strike-slip faults. In the Tangtse-Darbuk area, the Tangtse (SW) and Muglib (NE) mylonitic strands of the KSZ frame the less deformed Pangong Range. Inherited U/Pb ages show that granitic protoliths are mostly from the Karakorum and Ladakh batoliths, with a major Miocene melting event lasting from ≥21.5 to 13.5 Ma. Some of the Miocene granitic bodies show structural evidence for intrusion synkinematic to the KSZ. The oldest of these granitoids is 18.8 ± 0.4 Ma old, implying that deformation started prior to ~19 Ma. Microstructural data show that right-lateral deformation pursued during cooling. Ar/Ar data show that ductile deformation stopped earlier in the Tangtse (~11 Ma) than in the Muglib strand (~7 Ma). Deformation ended at ~11 Ma in the Tangtse strand while it is still active in the Muglib strand, suggesting a progressive localisation of deformation. When merged with published observations along the KFZ, these data suggest that the KFZ nucleated in the North Ayilari range at least ~22Ma ago. The long-term fault rate is 0.84 to 1.3 cm/yr, considering a total offset of 200 to 240 km. The KSZ collected magma produced within the shear zone and / or deeper in crust for which the producing mechanism stays unclear but was not the lower crustal channel flow.

1. Introduction

During continental collision, strain is partitioned into shortening and lateral extrusion [e.g., *Tapponnier, et al.*, 2001], but the relative importance of the two is debated. In the India-Asia collision zone, large and topographically marked thrusts and strike-slip faults are observed, and both thickening and lateral extrusion were important in accommodating the total shortening of ~1500- 2000 kilometres since 55 ±2 Ma [e.g., *Guillot, et al.*, 2003]. It remains debated, however, whether large strike-slip faults are transient structures that accommodate small amounts of total shortening, or major and long-lasting structures that play a long-standing role in the lateral extrusion of crustal or lithospheric- material. The main debate focuses on the duration of their movement, their total offset, and their depth extension (crustal or lithospheric). Some authors proposed that strike-slip shear zones are lithospheric features that accommodate large amounts of offset for long periods [e.g., *Avouac and Tapponnier*, 1993; *Peltzer and Tapponnier*, 1988; *Tapponnier, et al.*, 1986] whereas others proposed that these faults are transient structures, limited to the crust, that contribute to a distributed deformation [e.g., *England, et al.*, 1985; *England and McKenzie*, 1982; *Houseman and England*, 1993]. A related discussion concerns the way deformation localizes in a large strike-slip shear zone and the ability of such structures to produce and/or channel melts towards the surface [e.g., *Hutton and Reavy*, 1992; *Leech*, 2008; *Leloup, et al.*, 1999; *Paterson and Schmidt*, 1999]. Such debates are especially intense over the Karakorum fault zone (KFZ), which lies in the frontal part of the India-Asia orogeny, where crustal thickening is important and the thermal gradient is expected to be high [*Thompson and Connolly*, 1995], promoting distributed deformation rather than strain localization.

This paper presents new structural observations, 12 U/Pb ages and 24 Ar/Ar ages from the Tangtse region (NW-India), where deformed metamorphic rocks constituting the root of the KFZ are locally exhumed. We discuss the relationship between magma emplacement and deformation, and the way these relationships can be used to date the shear zone activity. We use new cooling histories of the main structural units to discuss the timing of deformation. This paper starts by a presentation of the KFZ and of the techniques used, before to present the new geochronology results and structural observations that allow to discuss the relationships between magmatism and deformation and the deformation migration within the shear zone. Finally, by integrating these results with published data from other portions of the KFZ, we evaluate its onset, the duration of ductile movement, and finally its propagation and long-term slip rate.

2. The Karakorum fault zone in the frame of the India – Eurasia collision.

In Ladakh, immediately East of the Nanga Parbat syntaxis, four main geological units have been described north of, and structurally above, the greater Himalayan sequences and the Tethyan sediments. These units are, from South to North, the Indus suture zone, the Ladakh batholith, the Shyok suture zone and the Karakorum batholith intrusive within the Karakorum metamorphic complex (KMC) [*Pêcher, et al.*, 2008]. These units are affected by south verging Tertiary thrusts, the most prominent ones being the Main Mantle thrust (MMT) at the base of the Indus suture zone, and the Main Karakorum thrust (MKT) at the base of the Shyok suture zone [*Weinberg, et al.*, 2000]. The units trend WNW-ESE and toward the east are deflected and / or truncated by the NW-SE right-lateral Karakorum fault zone (KFZ) [e.g., *Weinberg and Dunlap*, 2000], a prominent structure for which offsets, age and rates remain controversial. Correlation of some geological units across the KFZ in Tibet are not firmly established and offsets estimates range from null [*Jain and Singh*, 2008] to 1000 km [*Peltzer and Tapponnier*, 1988]. Nonetheless, the Tertiary Indus suture zone and the Mesozoic Ladakh batholith correspond to the Tsangpo suture zone and Gangdese batholith, respectively, suggesting a finite offset on the order of 200 [*Ratschbacher, et al.*, 1994] to 240 km [*Valli, et al.*, 2008].

The KFZ has a prominent morphological trace from Tash Gurgan in the NW to the Kailash area in the SE (Fig. 1b), related to recent and still active right-lateral motion of the Karakorum fault (KF), which has deflected the course of the Indus river by 120 km [*Gaudemer, et al.*, 1989] (Fig. 1b). However, the rate of recent motion and the active portion(s) of the fault are highly debated. From the offset of Quaternary moraines and fluvial terraces, slip rates of 10.7 ±0.7 mm/yr in the central portion (NA, Fig. 1b) [*Chevalier, et al.*, 2005], and >7–8 mm/yr along the southwest portion (Kailas, Fig. 1b) [*Chevalier, et al.*, 2012] have been determined. From GPS measurements [*Banerjee and Bürgmann*, 2002] argued for a present-day slip rate of 11 ±4 mm/yr. From the ^{10}Be dating of a single debris flow levee near Tangtse (T, Fig. 1b), [*Brown, et al.*, 2002] proposed a Quaternary slip rate of 4 ±1 mm/yr. Some even consider that the fault is no longer active, either north of its intersection with the active left-slip Longmu-Co Gozha-Co fault system [*Robinson*, 2009a], or along most of its length, as proposed from a GPS-derived rate of 3.4 ±5 mm/yr [*Jade, et al.*, 2004] and an InSaR-derived rate of 1 ±3 mm/yr [*Wright, et al.*, 2004].

Ductilely deformed rocks locally outcrop along the KFZ, (1) in the Nubra valley in India (P & S, Fig. 1b), (2) in the Darbuk Tangtse – Pangong region in India (D & T, Fig. 1b) and (3) in the Ayilari Range in China (NA, SA Fig. 1b). In all these locations the rocks show mylonitic textures with steep foliations and close to horizontal stretching lineations, with unambiguous right-lateral shear criteria [e.g., *Lacassin, et al.*, 2004; *Matte, et al.*, 1996; *Phillips and Searle*, 2007; *Rolland, et al.*, 2009; *Roy, et al.*, 2010; *Searle and Phillips*, 2007; *Searle, et al.*, 1998; *Valli, et al.*, 2007]. Because (1) the mylonites are parallel the KFZ for at least 400km, (2) the mylonites share the same direction and sense of motion as the KFZ, (3) there is no evidence for major tilting of the mylonites after their formation, these mylonites are interpreted as constituting the Karakorum shear zone (KSZ) corresponding to the exhumed deep part of the KFZ.

In the Tangtse zone (34°N, 78.2°E), the KFZ splits into two strands, which flank a topographic range, the Pangong Range, in which slightly deformed to mylonitized magmatic, migmatitic and metamorphic rocks outcrop (Fig. 2a). They constitute a metamorphic belt which exhibit a foliation trending N131° and plunging 84°SE on average, with a stretching lineation dipping from 20 to the SE to 40 to the NW (~15° to the NW on average) (Fig. 2b) as previously described [e.g., *Jain and Singh*, 2008; *Phillips and Searle*, 2007; *Rolland, et al.*, 2009; *Searle, et al.*, 1998]. Shear criteria indicate right-lateral shear. These rocks have been interpreted as the ~8 km-wide Kararakorum shear zone (KSZ) [e.g., *Rolland, et al.*, 2009; *Searle, et al.*, 1998]. Two main mylonitic strands bracket the Pangong range: the Tangtse strand to the SW and the Muglib strand to the NE. The exhumation of granulitic rocks (800°C and 5.5Kb) of the Pangong Range [*Rolland, et al.*, 2009], and their rapid cooling, has been related to right-lateral transpressive deformation between the two strands [*Dunlap, et al.*, 1998; *Mc Carthy and Weinberg*, 2010; *Rolland, et al.*, 2009].

Two valleys perpendicular to the belt give access to the structure of the KSZ: the Darbuk valley to the NW and the Tangtse gorge to the SE (Fig. 2). The sections expose from SW to NE: 1) The Ladakh batholith, 2) Rocks belonging to the Shyok suture zone including ultramafics and black mudstones containing Jurassic ammonoid fossils and volcano-clastic rocks [*Ehiro, et al.*, 2007]. These rocks are locally intruded by the ~18 Ma South Tangtse granite [*Leloup, et al.*, 2011]. 3) Mylonites of the Tangtse strand, with dextrally sheared mylonitic ortho- and para-derived gneisses and marbles, and leucocratic dykes parallel to the foliation as well as cross cutting ones. 4) The Pangong range where the country rocks and the leucocratic dykes appear less deformed. There, migmatisation affects both a metasedimentary sequence comprising Bt-psammites, calc-silicates and amphibolites, and a calc-alkaline granitoid suite comprising Bt-Hbl granodiorites, Bt-granodiorites, and diorites [*Reichardt, et al.*, 2010]. 5) The Muglib strand with dextrally sheared mylonites. 6) The Karakorum batholith and the Pangong metamorphic complex (PMC) comprising marbles and large (≥ 10 m) leucogranitic dykes, with foliations trending more easterly than in the KSZ, and locally showing left-lateral shear criteria [*Mc Carthy and Weinberg*, 2010]. Note that the various authors give different names to the geologic formations and that we use the names given in

Fig. 2.

In the Tangtse – Darbuk area, granitoids appear to have been formed during three major magmatic events. In the PMC sillimanite-grade metamorphism has been dated at ~108 Ma [*Streule, et al.*, 2009]. Such age has led to the interpretation that the PMC rocks belong to the Karakorum metamorphic complex found further NW in Pakistan across the KFZ (Fig. 1) [*Mc Carthy and Weinberg*, 2010; *Streule, et al.*, 2009]. In Pakistan the Lower Cretaceous calc-alkaline Karakorum axial Batholith (Fig. 1) formed during the northward subduction of the Shyok back-arc oceanic basin [e.g., *Rolland, et al.*, 2000]. The Karakorum metamorphic complex formed during this subduction and the following collision with the Kohistan-Ladakh arc prior to ~75 Ma [e.g., *Petterson and Windley*, 1985]. The Late Cretaceous Ladakh calc-alkaline batholith and the overlying Kardung volcanics emplaced between ~70 and 45 Ma above the northward subduction of the NeoTethys [*Dunlap and Wysoczanski*, 2002; *Ravikant, et al.*, 2009; *Upadhyay, et al.*, 2008]. Some granites and migmatites of the Pangong range have been dated between 108 and 61 Ma [*Jain and Singh*, 2008; *Ravikant, et al.*, 2009; *Reichardt, et al.*, 2010; *Searle, et al.*, 1998] (see Appendix F for details) and could be attributed to the Karakorum and/or the Ladakh Batholith. This latter outcrops ~10 km south west of the Pangong range (Fig. 1). The rocks outcropping between the Pangong range and the Ladakh granodiorites have been mapped either as part of this batholith (Khardung volcanics) [e.g., *Phillips, et al.*, 2004], or as belonging to the Shyok suture zone [e.g., *Ehiro, et al.*, 2007; *Ravikant, et al.*, 2009]. Within the Pangong range, a much younger magmatic event is revealed by numerous 14 to 21 Ma U/Pb ages of granitoids [*Jain and Singh*, 2008; *Phillips, et al.*, 2004; *Ravikant, et al.*, 2009; *Reichardt, et al.*, 2010; *Searle, et al.*, 1998] (see appendix F for details). Such magmatism has been related either to partial meting coeval with strike-slip deformation in the KFZ or to the Baltoro granite outcropping 150km farther NE across the KFZ (Fig. 1). This issue is discussed in details in section 6. Oligo-Miocene magmatic rocks (27-19 Ma) are also found ~100 km SW of the KFZ in the LeoPargill dome (LP, Fig. 1b) [*Langille et al., 2012*].

3. Analytical methods

In order to constrain the age of initiation and the kinematics of the KFZ, we conducted an integrated study, combining detailed structural analysis and U/Pb as well as Ar/Ar geochronology on variously deformed magmatic and metamorphic rocks.

3.1. Macrostructural, petrological and microstructural analysis

Geometry and intensity of ductile deformation is evaluated from field observations and laboratory analysis. A special attention was paid to the relationships between dykes and magmatic bodies emplacement with deformation. Oriented thin sections, cut perpendicular to the foliation (Z axis) and parallel to the lineation (X axis), corresponding to the XZ plane of finite strain, have been used for textural and microstructural studies of mylonites and dykes. The structures of deformed quartzo-feldspatic rocks such as granites depend on the metamorphic grade [e.g., *Passchier and Trouw*, 1998] allowing to evaluate the deformation conditions. Feldspar and quartz recrystallize at different temperature ranges, and the relationships between the weak recrystallized phase and the strong porphyroclasts are indicators of the deformation temperature. Quartz microstructures are commonly used to constrain the conditions of quartz deformation, particularly its temperature [*Hirth and Tullis*, 1991; *Stipp, et al.*, 2002; *Stipp, et al.*, 2006]. Quartz grains were studied in terms of shape, lattice preferred orientation (LPO), and dynamic recrystallization mechanism. LPO were measured with the Electron Back-Scattered Diffraction (EBSD) method in Geosciences Montpellier.

3.2. U/Pb geochronology

Zircons were separated using heavy liquids, a Frantz magnetic separator and finally by hand picking under a binocular microscope at the LGL-TPE (Université Lyon 1, France). Three samples were analysed with the SHRIMPII of the Geochronological laboratory of the Geological Survey of Canada, Ottawa (Canada) and the 9 others were analysed with the LA-ICP-MS of the Laboratoire Magma et Volcans, Clermont-Ferrand (France). When possible, both Tera-Wasserburg (TW) lower intercepts and Weighted average (WA) $^{206}Pb/^{238}U$ ages were calculated for each sample. For sets of concordant data, the WA age was preferred. Contrary to LA-ICP-MS, SHRIMPII analyses often required a common-lead correction, based on the ^{207}Pb isotope. The chosen age is the lower intercept $^{206}Pb/^{238}U$ age when a regression is calculated and the WA $^{206}Pb/^{238}U$ age otherwise. U/Pb data summary is given in Table 2, and most data are plotted on Fig.3, together with examples of analyzed zircons. The details of the analytical methods and settings are given in Appendix A and B for the SHRIMPII and LA-ICP-MS, respectively.

Given the high closure temperature (750-800°C) of the U/Pb system in zircons [*Clemens*, 2003], the ages mostly provide the timing of emplacement of the granitoids and in some cases the age of a previous melting event. When zircons show evidence of two crystallization stages, typically showing (1) cores having a different U-contents from the rims, underlined by different cathodoluminescence colours and/or (2) cores showing evidence of resorption and rims showing fine magmatic zoning in cathodoluminescence, the core ages are interpreted as inherited and the rim ages are interpreted as those of the last magma crystallization. Th/U ratios are calculated for each analysis. High Th/U ratios (>0.2) indicate an igneous origin for the zircons, whereas low Th/U ratios (<0.2) indicate that zircons grew in metamorphic or metasomatic conditions [*Rubatto, et al.*, 2001].

3.3. Ar/Ar geochronology

Analyses were performed on the 150-250 μm-size fraction after separation with Frantz magnetic separator, heavy liquids and finally by hand picking under a binocular microscope, carried out at the LGL-TPE (Lyon, France). We have analyzed 24 fractions of 16 samples in order to constrain the cooling history of the KFZ (Table 3). Ar–Ar ages were obtained at the geochronology laboratory of Geosciences Montpellier (University Montpellier 2, France). Analytical details are given in Appendix C. Ar/Ar data summary is given in Table 3, and plots in Fig.4.

Step heating was conducted using a classical furnace and yielded age spectra from which plateau and isochron ages were calculated and are shown side by side to assess potential excess Ar problems. If the inverse isochron age is close to the plateau age and if the $^{40}Ar/^{36}Ar$ ratio is not significantly different from the present day $^{40}Ar/^{36}Ar$ atmospheric ratio (295.5), we considered that the plateau age is reliable. When this is not the case, we used the inverse isochron age if it is well determined.

Once the age of a given mineral is calculated, a fundamental and controversial issue is to determine whether this age corresponds to mineral crystallization, recrystallization, or cooling below a given closure temperature. Near Tangtse, ductile deformation in the KSZ took place at temperatures above 500°C (see chapter 6), which is higher than the closure temperatures for the Ar/Ar radiogenic system of most minerals. Therefore $^{40}Ar/^{36}Ar$ ages are *a priori* interpreted to represent cooling ages, but we discuss if they can be interpreted differently. We built the cooling histories from our results and the bibliography. The closure temperatures are assumed to be 510 ±50°C for the amphiboles [*Harrison*, 1981], 390 ±45°C for the white micas [*Hames and Bowring*, 1994, and references therein], 320 ±40°C for biotites [*Harrison, et al.*, 1985]. K-feldspar modelling has also been used to infer T-t path in the Ayilari Range [*Valli, et al.*, 2007] and the Pangong Range [*Dunlap, et al.*, 1998].

4. Geochronological results

This section details the U/Pb and Ar/Ar geochronological data acquired for the Pangong area. The structural implications are discussed in sections 5 and 6.

4.1. U/Pb

Twelve variously deformed granitoids, including five granites and gneiss (LA12, LA18, LA29, LA33, LA34) and seven leucocratic dykes (LA13, LA14, LA17, LA25, LA28, LA58, LA60), were selected along the Tangtse and Muglib strands and across the KSZ for zircon U/Pb dating. The samples are located on Fig. 2 and listed in Table 1. The U/Pb results are presented below from the Tantgse strand (SW) to the Muglib strand (NE), listed in Table 2 and detailed in appendix D (Shrimp II) and E (LA-ICPMS). All published geochronological data from the KSZ are synthesized in appendix F.

LA25 and LA28 have been sampled in the south-western part of the Tangtse strand, close to the deformed part of the 18.5 Ma-old [*Leloup, et al.*, 2011] South Tangtse granite, in an outcrop that shows mylonitic gneiss interlayered with marble levels as well as amphibolitic and epidote rich skarn boudins (Fig. 5). Strongly deformed leucocratic dykes are parallel to the surrounding foliation, trending N130 72S with a stretching lineation with a pitch of 10W. While variously deformed dikes are oblique to the foliation, C/S structures in the gneiss indicate right-lateral shear. **LA25** is a strongly foliated aplitic dyke (Fig. 6a) showing alternating quartz and feldspar layers, underlined by biotite (Fig. 7g). Zircons are euhedral and transparent, have a typical magmatic zoning (Fig. 3a), and Th/U ratio typical of igneous zircons (0.2- 3.2). Four grains were dated, and the five common Pb-corrected ages, when plotted in the Tera-Wasserburg (TW) diagram, define a regression line with a lower intercept at 72.3 ±5.0 Ma (MSWD = 3.6) (Fig. 3a), interpreted as the emplacement age of LA25 protolith. Dyke **LA28** is sampled in the same outcrop as LA25 (Fig. 5a and b). It is a weakly foliated aplite, that crosscuts the N130-trending gneiss foliation, and that shows a slight necking suggesting it has been stretched after its emplacement (Fig. 6b). The stretching direction is compatible with the NW-SE right-lateral shear observed in the surrounding gneiss. In thin section the sample shows quartz, feldspar and rare biotite. Where biotite is present, it shows two dominant orientations that we interpret as C/S structures resulting from right-lateral shearing (Fig. 7d). Zircon grains are subhedral and transparent. They show regular growth zonation in cathodoluminescence imaging. Rims have Th/U ratio suggestive of a magmatic origin (0.1- 1.4). Some have a low-U homogeneous core with evidence of resorption (Fig. 3b). The only analysed core has a $^{206}Pb/^{238}U$ age of 435 ±5 Ma. The 6 rim data define a regression line in the TW diagram with an upper intercept anchored on the common Pb value, and a lower intercept at 18.8 ±0.4 Ma (MSWD=1.9, 4 zircons) (Fig. 3b), interpreted as the timing of the last crystallization event. Such age is similar within errors to the 18.6 ±0.2 Ma age of dyke LA20 sampled within the undeformed part of the South Tangtse granite [*Leloup, et al.*, 2011].

Few tens of meters northeast from LA25 and LA28, sample **LA29** (Fig. 5) is a mylonitic gneiss, with a N120, 65S trending foliation, a lineation pitch of 10W, that shows C/S dextral shear criteria. This gneiss has a metaluminous granitic composition, with an alternation of quartz, feldspar and biotite levels (Fig. 9f). Zircons of sample LA29 are euhedral and pink, with well-developed growth zoning (Fig. 3c) and high Th/U ratio (0.8 -1.8) typical of magmatic zircons. 21 spots were analyzed on 17 grains (cores and rims) and the resulting ages range between 68.8 and 73.3 Ma. No common Pb- correction were made for this sample because all the rims spots plot on, or slightly above, the concordia in a TW diagram, and define a regression line with a lower intercept at 71.3 ±0.6 Ma (MSWD=1.8)

(Fig.3a). This age is considered as the crystallization age of the protolith of this orthogneiss. This age is similar within errors to that of sample LA25.

Sample **LA33** belongs to a leucogranitic body, known as the "Tangtse granite" or "Tangtse mylonite" [*Jain and Singh*, 2008; *Searle, et al.*, 1998], that outcrops near the Tangtse monastery and prolongs to the NW across the Tangtse river. We call it the "Tangtse mylonitic orthogneiss" (Fig. 2 and Fig. 5). This two-micas and garnet-bearing orthogneiss, has been strongly mylonitized, the foliation trending N125 vertical and the stretching lineation having a pitch of 20 W. The mylonite shows feldspar porphyroclasts and recrystallized quartz ribbons, a clear right-lateral C/S fabric and σ-type porphyroclasts [*Searle, et al.*, 1998] (Fig. 9a). The occurrence of chlorite in the foliation evidences a greenshist facies overprint. Zircons of the Tangtse orthogneiss mylonite are transparent and euhedral and show a well-developed growth zonation. Some grains have low-U xenocrystic cores with evidence for resorption before the growth of the U-rich rims, indicating an inherited core surrounded by a younger rim (Fig. 3d). These rims display Th/U ratios between 0.03 and 0.51, which is intermediate between those of magmatic and metamorphic growth conditions [*Rubatto, et al.*, 2001]. 12 rim spots were analysed on 12 zircons and they plot slightly above the concordia in a TW diagram. They define two regression lines with lower intercepts at 15.8 ±0.5 Ma and 17.4 ± 0.4 Ma (Fig. 3d). The only analyzed core is concordant with a $^{206}Pb/^{238}U$ Upper Cretaceous age of 65.4 ±1.7 Ma. At the same location, [*Jain and Singh*, 2008] have obtained an older Upper Cretaceous U/Pb zircon age of 75.5±1 Ma (sample R7). Forty SHRIMPII $^{206}Pb/^{238}U$ zircons ages from the Tangtse mylonitic orthogneiss, sampled in an outcrop located two kilometres northwest-wards (sample 215, Fig. 2a), yield a complex age distribution with inherited cores showing a main population at 63±0.8 Ma, and core and rims between 15 and 21 Ma, for which a WA age of 18 ±0.6 Ma was proposed [*Searle, et al.*, 1998]. A single ID-TIMS age of 15.5±0.7 Ma was later calculated from one concordant zircon and two sub-concordant monazite fractions of the same mylonitic orthogneiss (sample P1) [*Phillips, et al.*, 2004]. We interpret the older ages of the Tangtse mylonitic orthogneiss as reflecting a Cretaceous inheritance, and the Miocene ages as reflecting several crystallization events, possibly starting as early as ~21 Ma, with the youngest ones at ~17 and ~15.5 Ma.

In the same area (Fig. 5), sample **LA34** belongs to a dark mylonitic biotite-rich gneiss containing small K-feldspar, with foliation trending N135, 78 SW and lineation with a pitch of 32 NW. This two micas and rare amphibole-bearing orthogneiss shows feldspar porphyroclasts and recrystallized quartz ribbons, both sharing clear right-lateral indicators such as recrystallization tails (Fig. 9c). Chlorite evidences a greenshist facies overprint. Zircons are similar to LA33's (Fig. 3e) and their Th/U ratios are indicative of magmatic origins (0.1- 2.1). A discordia regression has been calculated (10 analysis on 9 zircon rims) in the TW diagram, and the upper intercept provides an age of 19.1±2.9 Ma (MSWD = 2.0, Fig. 3e). One core has a $^{206}Pb/^{238}U$ age of 63.8 ±1.6 Ma, close to the inherited zircon age of the nearby Tangtse mylonitic Orthogneiss (LA33).

Ten kilometres north-westwards, the Darbuk granite is a NW–SE trending elongated stock of S-type peraluminous 2-mica gneissose granite [*Jain and Singh*, 2008], located along the north-eastern border of the Tangtse strand, near the Darbuk village (Fig. 2a). Its south-western margin is intensely sheared to granite mylonite, though the inner part remains poorly deformed. **LA18** was sampled in a zone where the granite is weakly deformed, with a vertical foliation trending N140. It is a fine-grained orthogneiss containing feldspar porphyroclasts recrystallized quartz, black and white mica (Fig. 9e). No clear shear criteria can be identified. Zircons display a typical core-and-rim structure in cathodoluminescence images (Fig. 3f). The rims display a mean intermediate Th/U ratio (0.01 to 0.3). 3 rim ages allow calculating a mean $^{206}Pb/^{238}U$ age of 17.9 ± 1.9 Ma (MSWD=9.9). This age is slightly younger than the average $^{206}Pb/^{238}U$ age of 20.8 ± 0.4 Ma obtained by [*Jain and Singh*, 2008] on zircon rims from the less deformed part of the granite, while corresponding core ages span between 45 and 671 Ma. Zircons from three deformed samples of the Darbuk granite [*Ravikant, et al.*, 2009] evidenced a large spread of ages, with the youngest concordant data interpreted to represent the last crystallization event at 19.1±1.1, 18.2±0.7 and 16.6±0.2 Ma. The Darbuk granite thus appears very similar to the Tangtse mylonitic orthogneiss.

To the NE, the Darbuk granite is in intrusive contact within right-laterally sheared dark gneisses mapped as a strongly foliated biotite diorite by [*Searle, et al.*, 1998]. In this unit, ~1km away from the Darbuk granite, sample LA12 (Fig. 2a) is an orthogneiss containing few euhedral hornblendes with a foliation trending N145 82S and a mineral lineation with a pitch of 37NW, showing right-lateral C/S structure underlined by feldspar porphyroclasts alternating with quartz and micas layers. The orthogneiss contains several leucocratic dykes either, parallel to, or oblique to the main foliation (Fig. 6d, e). Most dykes are deformed and show the same foliation as the surrounding gneiss. **LA12** zircons are pinkish with euhedral shapes and a fine zonation characteristic of magmatic growth (Fig. 3g). Their rims have a well-developed growth zonation with magmatic Th/U ratio (0.2- 0.7), and they commonly have low-U xenocrystic cores with evidence of resorption before the new growth phase (Fig. 3g). These cores display $^{206}Pb/^{238}U$ ages ranging from 25.6 to 22.8 Ma (10 analysis on 9 zircon cores), whereas the rims have a WA $^{206}Pb/^{238}U$ age of 21.5 ± 0.2 Ma (MSWD=1.4, 11 points on 11 grains) (Fig. 3f, g). The oldest core ages are interpreted as the onset of LA12 crystallization, while the WA age of the rims is considered as the final crystallization age. Samples LA13 and LA14 come from leucocratic dykes parallel to the orthogneiss foliation (Fig. 6d, e), that show a faint foliation (Fig. 7e, f). **LA13** has a granitic composition, showing large feldspar porphyroclasts surrounded by recrystallized quartz and mica (Fig. 7e). Zircons are strongly metamict and show uraninite exsolution (Fig. 3h). The Th/U ratio is high (0.3-

0.9), indicating a magmatic origin for the zircons rims. 9 rims analysis have been performed on 4 zircons and all rim points plot on the concordia in the TW diagram. The calculated intercept (MSWD=1.9) and the WA $^{206}Pb/^{238}U$ age are 14.2 ±0.1 Ma, interpreted as the crystallization age (Fig. 3h). The **LA14** leucocratic dyke has a granitic composition, showing feldspar porphyroclasts surrounded by recrystallized quartz and rare mica in thin section (Fig. 7f). LA14 contains transparent euhedral inclusions-rich zircons showing inhomogeneous cores and well-zoned magmatic rims in cathodoluminescence imaging. The Th/U contents of the rims are intermediate between those expected for metamorphic and magmatic zircons (0.07 to 0.69). Two cores display $^{206}Pb/^{238}U$ ages of 29.2 and 65.0 Ma, and the 15 rim ages define a regression line, which lower intercept in the TW diagram is at 14.8 ± 0.2Ma (MSWD=2.0, 11 zircons) (Fig. 3i). This age is taken as the crystallization age for this sample.

About ~700m south-west of the three previous samples, gneiss similar to LA12 with a foliation trending N170, 70W and a lineation pitch of 40N are cross-cut by an undeformed pegmatitic dyke from which **LA17** has been sampled (Fig. 6c). The dyke shows an irregular intrusive contact with the surrounding orthogneiss and do not show any evidence for deformation in thin section, with large undeformed quartz, white mica and feldspar (Fig. 7a). Pegmatite LA17 contains metamict zircons (Fig. 3j), similar to those previously described in sample LA13. The Th/U mean rim ratio is intermediate between those expected for magmatic and metamorphic crystallization conditions (0.02 to 0.66). All the rims spots (12 spots on 10 zircons) plot on, or slightly above, the concordia and define a regression line with a lower intercept at 14.7 ±0.3 Ma (MSWD = 0.8) (Fig. 3j), which is interpreted as the crystallization age.

12 kilometres to the SE, **LA48** has been sampled along the Tangtse gorge in an undeformed part of a granitic body of the Pangong range showing elsewhere heterogeneous deformation (Fig. 2a, b). This sample contains feldspar, quartz, biotite, some small epidote

and chlorite (Fig. 9g). It also contains pink euhedral zircons showing a typical magmatic-growth structure in cathodoluminescence imaging (Fig. 3k) and a magmatic U/Th ratio (0.1-2.5). 7 of the 17 analyses are discordant, and the TW age was calculated on the concordant data at 105.1 ±1.1 Ma (MSWD=1.2, 2 zircons) (Fig. 3k). This age is considered as the crystallization age.

Sample **LA58** was sampled along the Muglib strand, ~100m southeast of the North Muglib granite (Fig. 2a). There, leucocratic levels have been stretched and boudinaged parallel to the host schist foliation trending N135 vertical with a mineral lineation having a pitch of 5° SE. Some of the levels have sharp boundaries with the surrounding schists and the boudins asymmetry indicates a right-lateral shear sense. Other levels show more diffuse boundaries and contain some schist layers, but their asymmetry also indicate right-lateral shear (Fig. 6h, i). LA58 was taken from one of these levels. Despite this macroscopic deformation, the microscopic texture shows undeformed large minerals (feldspar, quartz, mica and garnet, Fig. 7c). Zircon grains are acicular, strongly metamict and show uraninite exsolutions (Fig. 3l). Their Th/U ratios are systematically low (≤ 0.03) and their U contents are very high: from 2200 to 15500 ppm. This implies that the rims crystallized in equilibrium with a fluid enriched in U and probably other fluid-soluble elements. Such high U content is a problem for SHRIMPII age determination because it has been shown that, whatever is the age and Pb contents of zircons, the Pb/U ratio measured with the SHRIMPII increases by 1.5 to 2 % for a U content above 1000ppm [*Williams, et al.*, 2000]. This analytical bias yields significantly older ages for U contents above 2000 ppm. In the case of LA58 the ^{207}Pb-corrected $^{206}Pb/^{238}U$ ages of zircon span from 13.2 to 18.6 Ma. A positive correlation between $^{206}Pb/^{238}U$ age and $^{238}U/^{196}Zr_2O$ (proxy for the U content) was used to infer a single corrected age of 15.4 ±0.4 Ma (6 measurements, MSWD =1.4- 6 grains) (Fig. 3l). This age is interpreted as the timing of crystallization of this leucocratic level.

4.2. Ar/Ar

Sixteen Ar/Ar ages were obtained on samples selected for U/Pb dating, in order to constrain the cooling history following their emplacement (Table 3): biotites from granitoids /gneiss (LA12, LA18, LA21, LA33, LA34 and LA48), and from dikes (LA13, LA14, LA25, LA28, LA58), and muscovites from some of the same samples (LA13, LA14, LA18, LA33, LA58). Five other samples (LA15, LA23, LA38, LA47, LA52) where selected to further constrain the cooling history, yielding four amphiboles, one muscovite and three biotite ages.

4.2.1. Micas

Of the 14 biotites dated, 4 yield plateau ages and 10 inverse isochron ages with $^{36}Ar/^{40}Ar$ ratio significantly different from that of the air (Fig. 4, Table 3). Biotite ages span from ~8.5 to ~13.7 Ma with a younging trend from SW to NE along the Tangtse section: 13.6 ±0.6 to 10.8 ±0.2 Ma in the South Tangtse granite and Tangtse strand (LA23, LA21, LA28, LA33, LA34 and LA38), 10.1±0.2 to 8.5±0.1 Ma in the central part of the section (LA48, LA12, LA13, LA14, LA18 and LA52), and 9.3±0.2 to 8.7±0.2 Ma in the Muglib strand (LA47, LA58) (Fig. 4, Table 3). These ages are comparable to the previously obtained age of 9.7 ±0.1 Ma in the North Muglib granite [sample 135 in *Dunlap, et al.*, 1998] (Appendix F, Fig. 2a). Outside of the Karakorum shear zone, Ar/Ar biotite ages are 11.3 ±0.2 Ma in the South Tangtse granite [sample 450 in *Searle, et al.*, 1998], and 10.6±0.3 Ma in the Pangong metamorphic complex [sample TNG45, *Mc Carthy and Weinberg*, 2010], (Appendix F, Fig. 2a).

Three of the 6 muscovite samples display ages older than the corresponding biotite ages: 9.7 ±0.2 Ma compared with 8.9 ± 0.1 Ma (LA18, Pangong Range), 10.7 ± 0.2 Ma compared with 9.3 ± 0.2 Ma (LA13, Pangong Range), and 9.9±0.2 Ma compared with 9.3 ±

0.2 Ma (LA58, Muglib strand), suggesting that the ages correspond to the mineral closure temperatures that is slightly higher for the muscovite than for the biotite. However, three muscovites display ages younger than the corresponding biotite ages: 10.7 ±0.1 Ma compared with 11.16 ± 0.17 (LA33, Tangtse strand), 7.1 ± 0.1 Ma compared with 8.9 ± 0.1 (LA14, Pangong Range), and 8.7±0.3 Ma compared with 8.7 ± 0.2 (LA47, Muglib strand) (Fig. 4, Table 3), suggesting that they have been affected by late reequilibration. Because these three rocks are deformed it is possible that such reequilibration occurred during deformation. Comparable ages were previously reported for muscovites in the Tangtse mylonitic orthogneiss (11.4 ±0.2 Ma, sample 128, [*Searle, et al.*, 1998]) and the Muglib strand (sample 217: 8.3±0.1 Ma, sample 130: 10.8±0.1 Ma, [*Dunlap, et al.*, 1998], Appendix F, Fig. 2a, Fig. 5).

4.2.2. Amphiboles

Of the 4 amphiboles dated, 3 yield plateau ages and 1 an inverse isochron age (Fig. 4, Table 3). From SW to NE, the three Ar/Ar amphibole ages are 17.8 ±0.5 Ma (LA23, south Tangtse Mountain), 19.7 ±0.3 Ma (LA38, Tangtse strand), 15.2 ±0.3 Ma (LA15, center of the Pangong Range) and 12.2 ±0.1 Ma (LA52, center of the Pangong range). In the Tangtse strand, the Ar/Ar age on amphibole of sample 129a [*Dunlap, et al.*, 1998] is significantly older than LA38: 29.6 ±0.3 Ma. Moreover, sample 129a did not yield any plateau age, but only a total fusion age, which is probably not significant. In the Pangong Range, two ages for amphibolites ~500m away from our sample LA52 give comparable ages: 13.6 ±0.9 Ma: [sample L441, *Rolland, et al.*, 2009], and 13.6±0.1 Ma [sample 212, *Dunlap, et al.*, 1998], (Appendix F, Fig. 2a, Fig. 5). In the Pangong metamorphic complex, amphiboles yield an age of 13.3 ±0.1 Ma [sample TNG45, *Mc Carthy and Weinberg*, 2010]. In each given sample or outcrop, the amphiboles are systematically older than the micas, which is logical given their respective closure temperature.

5. Constraining the age of onset and kinematics of the KSZ in the Darbuk – Tangtse area

The life span and general kinematics of the KFZ, especially in the Tangtse area, have been the matter of a debate that does not rest on differing geochronological data but on the interpretation of these data with respect to the timing of deformation. A first debate stands on the relationship between magma crystallization and strike-slip deformation, and a second one on the relationship between cooling and strike-slip shearing. In the following we re-evaluate these two aspects in the light of our new observations and geochronological data.

5.1. Evidence for synkinematic magmatism and implications for the onset age and localisation of deformation.

5.1.1 Debate on the coevality between Miocene magmatism and right-lateral deformation.

While numerous evidences for Miocene magmatism in the Tangtse area have been published, there is no consensus on whether this magmatism is coeval, or not, with the KFZ. Two opposing views have been proposed. Some advocate for a main magmatic phase antecedent to the onset of deformation and few leucocratic dykes emplacement after that deformation [e.g., *Phillips, et al.*, 2004; *Searle and Phillips*, 2007], while other think that at least part of the magmatism was coeval to strike-slip deformation [e.g., *Hasalova, et al.*, 2011; *Leloup, et al.*, 2011; *Reichardt and Weinberg*, 2011; *Weinberg, et al.*, 2009; *Weinberg and Mark*, 2008].

In the Tangtse strand, some authors have distinguished two sets of Miocene magmatic rocks. The first set consists of mylonitic leucogranites and leucocratic dikes concordant to the foliation of the KSZ and the second to undeformed leucocratic dikes that crosscut that foliation [*Phillips, et al.*, 2004; *Searle and Phillips*, 2007]. Because there where no evident textural criteria for high temperature deformation within rocks of the first set, their crystallization ages of 15.55 ±0.74 Ma (sample P1 – Tangtse mylonitic orthogneiss) and 15.63±0.52 (sample P11) have been interpreted as defining a maximum age for the initiation of ductile deformation [*Phillips, et al.*, 2004]. The age of sample P8 from the second set would indicate that ductile deformation ceased prior to 13.72±0.18 Ma. Near Satti and Panamik, ~100 km NW along strike (S & P, Fig. 1b), one mylonitic leucogranite crystallized at 15.87±0.08 Ma (P38), while one crosscutting dike is 13.73±0.34 Ma old (P37) [*Phillips, et al.*, 2004]. These ages appear to confirm that ductile deformation started after ~15.5 and ended prior to 13.7 Ma in the KSZ [*Phillips, et al.*, 2004]. A structural study confirmed that the Tangtse mylonites have not exceeded greenschist–lower amphibolite facies, and that there is no evidence for submagmatic deformation nor structural indicators that would suggest synkinematic magmatism [*Phillips and Searle*, 2007].

On the opposite, some authors proposed that some Miocene magmatic rocks emplaced coevally to the KSZ shearing in the Tangtse region. The South Tangtse granite (Fig. 5b) presents all characteristics of a synkinematic pluton that would have emplaced at the southern margin of the Tangtse strand [*Leloup, et al.*, 2011]. The South Tangtse granite shows a progressive transition from an undeformed granite in its central part, to a granite with a faint magmatic foliation, and finally a mylonitic orthogneiss in the Tangtse strand (Fig. 5). The fact that the magmatic fabric is parallel to the mylonitic one suggests that the ~18.5 Ma old granite crystallization (18.5±0.2 Ma, granite LA21 and 18.6 ±0.2 Ma, undeformed dike LA20) was coeval with the right-lateral deformation [*Leloup, et al.*, 2011].

Other authors have proposed that melting and magma migration within the Pangong range was coeval to the right-lateral shearing [*Hasalova, et al.*, 2011; *Reichardt and Weinberg*, 2011; *Weinberg, et al.*, 2009; *Weinberg and Mark*, 2008]. In the Pangong Range, migmatitic magmas formed by local anatexis and migrated during folding into axial-planar leucosomes [*Weinberg and Mark*, 2008]. As these steep axial planes trending N120 to N140 are sub-parallel to the mylonitic foliation in the two strands framing the Pangong range it was concluded that anatexis, folding and right-lateral shearing where coeval [*Weinberg, et al.*, 2009; *Weinberg and Mark*, 2008]. At a macroscopic scale, the close relationship of the dyke network with the structures resulting from right-lateral shear lead [*Reichardt and Weinberg*, 2011] to propose that magma migration was controlled by stresses related to right-lateral transpression. At a microscopic scale, [*Hasalova, et al.*, 2011] showed that late melt channels follow two distinct orientations, parallel to the S-C fabric resulting from right-lateral shear in the KSZ, thus implying that magma migration was coeval with the deformation. It is worth to note that none of the Miocene intrusions shows structures that could suggest it has been emplaced with a dip significantly different from its present day geometry.

The field relationships between magma intrusion, crystallization and right-lateral deformation in the KSZ thus appear more complex than those proposed by [*Phillips, et al.*, 2004] and [*Searle and Phillips*, 2007], justifying further re-examination of some of the field evidences.

5.1.2. Tangtse strand: a re-examination of the structural relationships

The most spectacular outcrops of right-lateral mylonitic marbles, calcsilicates and orthogneiss are found on the Tangtse strand of the KFZ, around the Tangtse monastery located on the right bank of the Tangtse river (Fig. 5a). Two of the five dykes interpreted as purely pre- or postkinematic by [*Phillips, et al.*, 2004] (P8 and P11, Fig. 5a) are located in this outcrop, which is key to discuss the structural relationship between magmatism and deformation.

P8 is a leucogranite dike displaying a moderate foliation and that crosscuts the foliation of the surrounding gneiss [*Phillips, et al.*, 2004] (Fig. 6f). These gneisses strike N120 to N130, 80 SW with a lineation with a pitch of 15 to 35 NW (Fig. 5a). A SW-NE cross-section across the outcrop exhibits successively, amphibolite, marble and skarn boudins and slivers, dark gneiss, and the Tangtse mylonitic orthogneiss (Fig. 5a). Granites and skarns are found as boudins in the amphibolite and marbles, and mylonitic leucocratic dikes are concordant to the foliation. The whole series is affected by intense NW-SE right-lateral shear. U/Pb zircon ages of LA34 (19.0 ±2.9 Ma), LA33 (17.4±0.4 and 15.8±0.5) and P11 (15.6±0.5) [This study, *Phillips, et al.*, 2004] indicate that deformation affected granite that crystallised between ~19 and ~15 Ma. In the absence of unequivocal microstructural evidences for syn-melting deformation these ages do not constrain the timing of initiation of the shearing deformation. However a close examination of the dyke P8 that is supposed to seal the deformation reveals that, if it is indeed crosscutting the foliation formed by right-lateral shear for ~8m, both its extremities are deformed and form asymmetric tails resulting from right-lateral ductile deformation (Fig. 6f, g). This implies that this intrusion is not postkinematic but synkinematic, and thus that deformation was going on, not finished, at ~13.7 Ma.

About 200 m south-westwards, at the foot of the South Tangtse Mount, strike-slip deformation affects Cretaceous granites (e.g., LA29, 70.8 ±0.5 Ma) and dikes (e.g., LA25, 71.1 ±0.8 Ma), as well as the NE margin of the syntectonic South Tangtse granite (Fig. 5). At this location, sample LA28 is from a dyke that crosscuts the foliation (Fig. 6b) but that is itself deformed by the right-lateral shearing, as shown by its stretching (Fig. 6b) and its internal foliation (Fig. 7d) parallel to that of the host gneiss. These features suggest that LA28 is synkinematic to the right-lateral shear and that its age of 18.9 ±0.5 Ma is a minimum age for the deformation onset.

Combining the ages of the granitoids for which there are structural evidences for syn-deformation crystallization (P8 and LA28) suggests that ductile deformation in the Tangtse strand occurred at least from ~19 to ~14 Ma (Fig. 8). If this true, this would imply that most dated granitoids of the Tangtse strand are synkinematic of deformation.

5.1.3. Miocene magmatism and deformation heterogeneity in the KSZ near Tangtse.

Deformation intensity is often used as an indicator of relative ages between intrusive rocks. However, this neglects the possibility that deformation is heterogeneously distributed. In the Tangtse strand there are examples of weakly strained rocks that are older than more intensely sheared rocks. For instance the undeformed dyke LA60 (16.0 ± 0.6 Ma) [*Leloup, et al.*, 2011]) crosscutting the right-lateral foliation has the same age as some nearby deformed granitoids of the Tangtse strand that could be interpreted as prekinematic, such as sample P11, LA33 and P1 (Fig. 8). In the same way, synkinematic intrusions at the SW border of the Tangtse strand (LA28, LA21 and LA20) have similar or older ages than ones that could be interpreted as prekinematic, as for example the Tangtse mylonitic orthogneiss (Fig. 8). Such pattern would seem incoherent if the deformation was homogeneous in space and time within the shear zone, and if the intrusions were considered as strictly pre- or postkinematic. However, the age pattern is easily explained if deformation was not homogeneous within the Tangtse strand of the KSZ, and had migrated through time. The minimum time span for right-lateral deformation in the Tangtse strand is bracketed by the oldest and the youngest synkinematic intrusions between 18.9 ±0.5 (LA28) and 13.7 ±0.2 (P8) Ma (see previous section). All the intrusions that emplaced in the KSZ in the Tangtse area during this time span are synkinematic of the KSZ, even if they are undeformed. This time span encompasses the ages of all Miocene intrusions within the Tangtse strand and 13 out of the 15 Miocene dated granitoids of the Pangong range and Muglib strand (Fig. 8).

In the Pangong range, where the deformation linked to the KSZ appears milder, granitoids have yield three main groups of U/Pb ages. The oldest group span between 108 and ~104 Ma ([*Phillips and Searle*, 2007; *Searle, et al.*, 1998]; and LA48, this study), the second between ~74 and ~55 Ma [*Jain and Singh*, 2008; *Ravikant, et al.*, 2009; *Reichardt, et al.*, 2010], and the youngest between ~22 and ~14 Ma [*Jain and Singh*, 2008; *Phillips*, 2004, this study; *Ravikant, et al.*, 2009; *Reichardt, et al.*, 2010], (Fig. 8, Table 2, Appendix F). Following *Searle, et al.* [1998] and *Reichardt, et al.* [2010], we interpret the two oldest ages groups to indicate that granitoids of the Karakorum and Ladakh batholiths may have not melted since their emplacement, and/or that zircons of the two batholiths have been incorporated in some Miocene granitic intrusions parental melts. Upper Cretaceous inherited ages are also occasionally found in the Tangtse strand [*Jain and Singh*, 2008, this study].

The youngest age group corresponds to a Miocene magmatic episode for which field relations, detailed structural analysis and isotopic analysis suggest widespread partial melting of two major rock sequences, meta-sedimentary and calc-alkaline rocks, in the presence of a water-rich fluid contemporaneously with right-lateral deformation [*Hasalova, et al.*, 2011; *Reichardt and Weinberg*, 2011; *Reichardt, et al.*, 2010; *Weinberg, et al.*, 2009; *Weinberg and Mark*, 2008]. For example, the North Muglib granite (called « Tangtse granite » by several authors), that crystallized between 18.0 ±0.4 Ma (U/Pb zircon and titanite, sample TNG148a), [*Reichardt, et al.*, 2010] and 15.1 ±0.6 Ma (U/Pb zircon, monazite, xenotime, sample P46), [*Phillips and Searle*, 2007], is interpreted to have crystallized during right-lateral shear in a pressure shadow of the competent ~71Ma old South Muglib granite [*Reichardt, et al.*, 2010; *Weinberg, et al.*, 2009].

Further northwest in the Pangong range, the Darbuk granite (Fig. 2a) is undeformed in its central part and becomes mylonitic at its margins with foliation trending N145, 52SW. The deformed part of the Darbuk granite yields 17.9 ±1.9 Ma old zircons (LA18, Fig. 3g). Together with the previously obtained ages ranging between 20.8 ±0.4 and 16.6±0.2 Ma from samples SY46 [*Jain and Singh*, 2008], and DT20, DT-7, N-8 [*Ravikant*, *et al.*, 2009], this age suggest a protracted period of crystallization between ~21 and ~16 Ma for the Darbuk granite (Fig. 8). To the NE, the Darbuk granite intrudes right-laterally sheared dark gneisses (LA12), which have undergone a protracted melting event between ~26 and 22 Ma (Fig. 3f and Fig. 8). Both the gneiss and the deformed granite are intruded by several generations of leucocratic and pegmatitic dykes. Within the gneiss, two dykes (LA13 pegmatite, LA14 aplite) stretched parallel to the right-lateral foliation (Fig. 6d, e) are located ~700m from an undeformed pegmatite that cross-cuts the right-lateral foliation (LA17) (Fig. 6c and 7a). The three dykes yield nearly identical U/Pb zircon ages: 14.2 ±0.1, 14.8 ±0.2 Ma and 14.7 ±0.3 Ma, respectively (Fig. 3i, k, l, and Fig. 8), the deformed dyke LA13 being slightly younger than the undeformed one (Fig. 8). This suggests that all three dykes are synkinematic, but that deformation continued after ~14.5 Ma at the location of LA13, LA14 while it was already over at the location of LA17, or was not recorded by this dyke due to rheological heterogeneities.

In the Muglib strand, the pegmatitic dyke LA58, located ~100m south-east of the North Muglib granite (Fig. 2), shows asymmetric boudinage deformation related to the KSZ (Fig. 6h & i) within micaschists trending N135 vertical with a lineation with a pitch of 5° to the SE. The pegmatite shows little internal deformation (Fig. 7c). The melt embeds schist layers similar to those constituting the surrounding gneiss (Fig. 6h & i). This suggests that the melt formed as the foliation was already present and thus that it is synkinematic. The U/Pb zircon age of this sample (15.4 ±0.4 Ma, Fig. 3J, Table 2) implies that ductile deformation was going on at ~15 Ma at this location (Fig. 8). A nearby deformed granitoid yielded a 15.1±0.6 Ma (P46) [*Phillips*, 2004] U/Pb age, confirming that deformation lasted after ~15 Ma in the Muglib strand (Fig. 8).

The picture that emerges for the Pangong range and Muglib strand is similar to that of the Tangtse strand: rocks of the Karakorum and Ladakh batholith, as well as sedimentary series, undergoing partial melting since ~25Ma, and heterogeneous right-lateral deformation from at least ~18 Ma, until at least ~15 Ma. On a more methodological point of view, one may observe that in such shear zone, constraining the onset of deformation requires a large chronological data set, and can be hindered by the fact that structural evidence for syntectonism can be overprinted by latter deformation. Deformation could migrate within the shear zone because of synkinematic intrusions, which modify the local rheology. It has been shown that shear deformation tends to localize within low-resistance shear bands such as weak dykes or along rheological boundaries [e.g., *Mancktelow and Pennacchioni*, 2005; *Pennacchioni and Mancktelow*, 2007]. We suggest that the same process is active in mylonites, which are typically rheologically-inhomogeneous zones, particularly when magmatism and deformation are synchronous. Concurrently, cooling could probably also tend to promote strain localization, and this process will be discussed in more details further down this section.

5.2. Cooling during continuous deformation

Beside the relationships between intruding magmas and deformation, the relationships between the temperature evolution and deformation can be investigated through the microstructures and also yields important constraints on the timing of deformation. Such analysis has already been conducted [*Phillips and Searle*, 2007; *Rolland, et al.*, 2009; *Roy, et al.*, 2010] and our observation are essentially similar. However our conclusions on the highest temperature of deformation differ significantly from those of [*Phillips and Searle*, 2007] and [*Roy, et al.*, 2010].

5.2.1. Microstructural evidence for continuous shearing during cooling

Right-laterally sheared gneiss samples LA12, LA33, and LA34, have feldspar porphyroclasts commonly showing recrystallized grains at their boundaries, producing a core-and-mantle structure, diagnostic of dynamic recrystallization [e.g., *Passchier and Trouw*, 1998], whereas quartz is entirely recrystallized (Fig. 9 a -d). Such dynamic recrystallization strongly depends upon temperature, and to a minor extent on other factors (strain rate, differential stress, and the chemical activity of water) [*Passchier and Trouw*, 1998; *White*, 1975]. Consistent observations in several natural examples suggest that dynamic recrystallization of both quartz and feldspar occurs during deformation at temperature above 600–500°C [*Gapais*, 1989; *Leloup, et al.*, 1995; *Passchier and Trouw*, 1998]. Mylonitized leucocratic dyke LA29 (Fig. 9f) shows alternating quartz and feldspar layers, which are also diagnostic of high-grade conditions in which quartz and feldspar are both weak phases with easy dislocation climb and recovery [*Passchier and Trouw*, 1998, and references therein]. It is important to note that LA12, LA33, and LA34 have experienced a Miocene phase of melting and zircon crystallization, whereas LA29 did not melt since the Cretaceous. Nevertheless all these rocks share high temperature microstuctures.

Other deformation characteristics indicate that deformation continued under retrograde conditions, as described by [*Rutter, et al.*, 2007] for marbles. Abundant myrmekite grew along the boundaries of K-feldspar porphyroclasts (Fig.9b-e), especially at high stress sites, suggesting a deformation under medium-grade temperature conditions (400 – 600°C) [*Gapais*, 1989; *Gates and Glover*, 1989; *Passchier and Trouw*, 1998; *Simpson and Wintsch*, 1989; *Tsurumi, et al.*, 2003; *Tullis and Yund*, 1987]. Bent twin lamellae (Fig.9b) and undulose extinction in feldspar porphyroclasts when quartz still deforms ductilely suggest deformation under lower-grade temperature conditions (300–400°C), [e.g., *Gower and Simpson*, 1992; *Jensen and Starkey*, 1985; *Ji and Mainprice*, 1990; *Olesen*, 1987; *Olsen and Kohlstedt*, 1985; *White and Mawer*, 1986]. Brittle deformation of feldspar porphyroclasts, with microfractures filled by late micas (Fig.9b), indicates even lower-grade conditions (<300°C) [*Passchier and Trouw*, 1998; *Tullis and Yund*, 1987] during late increments of deformation. Micas also show characters typical of very low-grade metamorphism below ~250°C, such as undulose extinction [*Stesky*, 1978; *Stesky, et al.*, 1974].

The solid-state deformation microstructures shows that the samples were right-laterally sheared from around 600°C down to <250°C. The absence of a higher temperature fabric does not demonstrate that none of these samples experienced deformation at higher temperature, i.e. when melt was present, because a solid-state deformation fabric may have been superimposed and erased any earlier magmatic fabric. In fact, as mentioned in section 5.1.1., *Hasalova, et al.* [2011] describe microstructures that attest for coeval magma migration and right-lateral deformation.

5.2.2. Quartz microstructures and conditions of deformation.

Quartz ribbons from three samples have been studied. LA59 was sampled close to LA58, the dated synkinematic pegmatite of the Muglib stand. LA30 is a quartz ribbon, sampled in the amphibolitic mylonites at the foot of the Tangtse monastery, in a sheared greenschist (N125, 65S, lineation pitch: 20W). LA26 was sampled in the same outcrop as LA25/LA28 at the SW margin of the Tangtse strand (Fig.5), where the foliation trends N120, 65S (lineation pitch: 10W). These ribbons probably formed by mineral segregation during the right-lateral deformation and define mono-mineralic centimetre-wide layers where quartz recrystallized without any interference from other minerals with different competence.

Sample LA59 contains large and irregular recrystallized grains with lobed boundaries (Fig.10c), which are typical of grain boundary migration (GBM) recrystallization mechanism. GBM is a high-temperature, low-stress mechanism (>500-550°C) [*Hirth and Tullis*, 1991; *Stipp, et al.*, 2002], where highly deformed older grains are replaced by relatively undeformed grains via the migration of their boundaries. This high temperature deformation is confirmed by the lattice preferred orientation of the grains. In the stereographic plot of the <c> axis orientations measured by Electron Back Scatter Diffraction (Fig. 10c), the density maximum is located in the centre, showing that prism <a> is the preferentially activated slip system, during quartz deformation. This prismatic <a> slip occurs at medium to high temperature conditions (500 -600°C) [*Gapais and Barbarin*, 1986; *Mainprice, et al.*, 1986; *Stipp, et al.*, 2002]. The same kind of lobed grains are observed in sample LA26 (Fig.10a), and the LPO is also consistent with a prismatic <a> slip activation. Therefore, we infer that the two samples (LA26 – Tangtse strand and LA59 – Muglib strand) have been deformed at temperatures higher than 500°C.

The larger grains of quartz in samples LA26 and LA59 also show undulose extinction and sub-grains, indicating that they are themselves deformed, and for LA26, smaller polygonal grains recrystallize at their boundaries. The recrystallization mechanism involved here is the sub-grain rotation (SGR) [*Hirth and Tullis*, 1991; *Stipp, et al.*, 2002], that occurs at medium temperature (400-500°C) [*Stipp, et al.*, 2002] and medium stress conditions, and is characterized by disorientation of some parts of a quartz grain by concentration of dislocations into walls.

SGR is the dominant mechanism in sample LA30 (Fig10b): most of the grains are small (<100μm) and polygonal, located around or within larger grains that show strong undulose extinction and sub-grains. However, quartz LPO indicates that the prismatic <a> slip has also been activated in sample LA30, suggesting deformation at T>500°C (Fig. 10b).

In such case, the absence of GBM texture could be due to a later complete SGR recrystallization at 400°C<T<500°C, without impacting on the <c>-axis fabric.

In summary, the three investigated samples, from the two stands of the KSZ, thus demonstrate right-lateral shearing above 500°C.

5.3. Thermochronology and P-T-t-deformation paths

The different temperature-dependent deformation mechanisms described above produce asymmetric microstructures indicating sense of shear. Sigmoidal feldspar recrystallization, myrmekite formation at high stress sites (Fig. 9), quartz shape orientations and LPO (Fig. 10), and asymmetric mica fishes all indicate the same unambiguous dextral shear sense. Such dextral shear thus appears to have been continuous from temperatures higher than 600°C down to low-grade conditions of <250°C. This cooling can be dated by using the Ar/Ar method combining the various minerals that have closure temperature ranging from ~500 to ~150°C.

The cooling history of the KSZ can be constrained by combining the U/Pb ages with the 10 previously published Ar/Ar data [*Dunlap, et al.*, 1998; *Mc Carthy and Weinberg*, 2010; *Rolland, et al.*, 2009], and the 24 new Ar/Ar data from this study (section 4.2, Table 3, Appendix F). Most data are compatible with each other if interpreted as reflecting the closure temperatures of each mineral species, and if one takes into account the presence of four different structural units (a- South Tangtse granite, b- Tangtse strand, c- Pangong Range and d- Muglib strand; Fig. 11). The U/Pb ages correspond to high temperature in the crystallizing melt (750-800°C), but the regional significance of such temperature depends on the size of the pluton. Small dykes may have intruded into much colder rocks and we have arbitrarily plotted them at ~700°C, but the actual temperature of the country rock may have been anywhere between ~500 and 800°C. For the Ar/Ar ages, only amphibole 129A (from an amphibolitic pod within the calcmylonites) with a total fusion age of 29.6 ±0.3 Ma [*Dunlap, et al.*, 1998], appears significantly older that what would be expected for a simple cooling after the time of granites emplacement (Fig. 11b). We note however that this amphibole did not yield a plateau age and that our sample LA38 collected nearby gives a much younger age (19.68 ±0.28 Ma). On the other hand, the two available K-feldspar T-t paths inferred from multi-domain diffusion modelling [*Dunlap, et al.*, 1998] fit well with the other available data (Fig. 11b & d).

Our Ar/Ar data confirm that the KSZ cooled later than the surrounding terranes. For example, the Ladakh batholith to the South (Fig. 1b) cooled below 150°C by the late Oligocene (30 Ma) [*Clift, et al.*, 2002; *Dunlap, et al.*, 1998]. Miocene cooling of the KSZ is rapid: 40 to 80°C/Ma on average, as measured from the T-t paths between ~800 and ~300°C. As suggested by the raw data, cooling below ~400°C, indicated by the micas ages, occurs diachronously across strike: at ~14 Ma in the Tangtse strand and at ~11 Ma in the Muglib strand (Fig. 11). Such cooling pattern could result from an earlier exhumation of the SW (Tangtse) side of the shear zone, which is compatible with a reverse fault component of the right-lateral deformation suggested by the NW dip of the lineations in that zone (Fig. 5a).

In each structural zone, comparison of the temperature range for syntectonic cooling deduced from structural analysis (Fig.11e) with the cooling history (Fig. 11a, b, c, d) allows to deduce the time range for right-lateral ductile deformation: ≥18.5 to ~14 Ma for the South Tangtse mountain, ≥19 to ~11 Ma in the Tangtse strand and ≥15 Ma to ~7 Ma in the Muglib strand. The few muscovite ages that could be interpreted as dating deformation rather than cooling (LA33, LA14 and LA47, see section 4.2.1) are compatible with these time ranges (Fig. 11). It is worth to note that if the U/Pb data are discarded as dating deformation, the analysis of the Ar/Ar data alone suggests that deformation started prior to ~17 Ma in the

South Tangtse Mountain, ~20 Ma in the Tangtse strand, ~15 Ma in the Pangong range, and ~13Ma in the Muglib strand (Fig. 11).

The only available P-T path for the KSZ have been obtained from the Pangong range (samples L441 and L212) [*Rolland, et al.*, 2009]. Combination of the P-T path proposed by [*Rolland, et al.*, 2009] with our T-t path (Fig. 11c), allows building a P-T-t path for the Pangong range unit (Fig. 11f). According to this path, at least ~20 km of exhumation occurred during the right-lateral deformation. About 40% of that exhumation occurred before 12 Ma, while deformation was still ductile, at a mean rate of ~1mm/yr. Exhumation of the Pangong range has been attributed to transpressive deformation [*Dunlap, et al.*, 1998; *Mc Carthy and Weinberg*, 2010; *Rolland, et al.*, 2009]. The NW dip of the lineation implies a vertical motion of the Pangong range relative to the Shyok suture zone / South Tangtse granite during the right-lateral deformation. For the average dip of ~15° this vertical motion would correspond to ~27% of the horizontal motion, and an exhumation of ~20 km could corresponds to ~75 km of horizontal offset. However lineations show various dips from 20° SE to 40° NW and it is impossible to attribute a given dip to a precise time period. It is thus impossible to constrain more precisely what would be the horizontal motion needed to explain 20 km of exhumation. During this exhumation, the apparent geothermal gradient, considered as linear in the conductive crust, progressively decreased from > 40° km^{-1} to "normal" geothermal conditions prevailing in an unperturbed lithosphere of ~30° km^{-1}. The initially high geothermal gradient may have been due to heat advection by rising melts or fluids, as suggested by the abundance of granitic magmatism between ca. 20 and ca. 15 Ma. The peak P-T conditions and the associated high apparent thermal gradient are close to those observed in other major strike-slip ductile shear zones as for example the ASRR [*Leloup, et al.*, 2001; *Leloup, et al.*, 1999].

6. Karakorum Fault Zone: initiation and evolution

Our new data in the Tangtse area shed light on several controversial issues on the KFZ, and its ductile root, the KSZ in particular, and large strike-slip shear zones in general. The first point is the relationship between deformation and magma generation and/or migration. The second point is the age of initiation, the kinematics of propagation and the long-term fault rate on the KFZ. The third and last point is the way deformation localizes in large shear zones.

6.1. Relationships between magmatism and deformation in the KSZ

An intimate link has long been proposed between large strike-slip faults affecting the continental crust and magmatism [e. g., *Hutton and Reavy*, 1992; *Leloup, et al.*, 1999 and references therein]. In the KSZ such, link has been proposed based on field and microstructural observations attesting for synkinematic magmatism in the Tangtse area [*Lacassin, et al.*, 2004; *Leloup, et al.*, 2011; *Reichardt and Weinberg*, 2011; *Reichardt, et al.*, 2010; *Rolland, et al.*, 2009; *Valli, et al.*, 2008; *Weinberg, et al.*, 2009; *Weinberg and Mark*, 2008]. The same relationship has been proposed farther southeast in the North Ayilari range, where a mildly deformed dyke that crosscuts the right-lateral foliation, which has thus been interpreted as synkinematic, yielded a zircon U/Pb age of 22.7±0.1 Ma (Sample C32) [*Lacassin, et al.*, 2004; *Valli, et al.*, 2008]. In the same area, biotite-hornblende mylonitic granites with interbedded felsic bands, indicating at least partial melting during intensive dextral shearing, yielded zircons with an U/Pb age of 18.72±0.42 Ma (Sample A2) [*Wang, et al.*, 2011]. However, other authors contest the evidence for synkinematic magmatism and high-temperature deformation and propose that magmatism occurred only before or after deformation [e.g., *Phillips, et al.*, 2004; *Searle and Phillips*, 2007; *Wang, et al.*, 2009]. In this contribution we have presented further evidences that demonstrate that most of the Miocene magmatism in Tangtse was emplaced within, or along, the shear zone at the time of deformation. This confirms the interpretation that at least part of the magmatism was synkinematic in the central section of the KFZ (Fig. 12). This does not prove that all Miocene magmatism in the KFZ is synkinematic. Actually, it may be very difficult to determine if the oldest Miocene melts (e.g. LA12 in Tangtse and P18 in North Ayilari) were syntectonic or not. This is because within the shear zone, field evidence for syntectonic magmatism are difficult to find as early structures are overprinted by later deformation. Furthermore, as neither magmatism nor deformation were homogeneous in space and time within a shear zone affecting older (Cretaceous to Eocene) granitoids, a large number of ages together with precise structural constraints will be needed in order to get the full picture of the deformation history.

The timing relationship between right lateral shearing and magmatism does not necessarily imply a causal relationship, and several mechanisms may be envisaged to generate melts in strike-slip shear zones. 1) Magmas could be generated within the fault zone by shear heating either in the crust [e.g., *Molnar and England*, 1990; *Nicolas, et al.*, 1977] or in the upper mantle [e.g., *Leloup and Kienast*, 1993; *Leloup, et al.*, 1999]; 2) Vertical motion within the dominantly strike-slip deformation zone could have induced heat advection [*Leloup, et al.*, 1999] and/or decompression melting [*Rocchi, et al.*, 2003; *Zhang and Schärer*, 1999]; 3) the fault zone could act as a preferential channel for fluids generated by another mechanism, such as crustal thickening [e.g., *Huerta, et al.*, 1998] or channel flow [*Leech*, 2008]; 4) stress concentration in “process zones” associated to shear zones could be the locus of large energy dissipation [*Deves, et al.*, 2011].

Beside the timing of deformation and melting, our new data bring few hints to discriminate between these mechanisms. According to the thermal-mechanical model for shear heating along large strike-slip faults proposed by Leloup et al. [1999], a fault rate on the order of ~10 mm/yr (see section 6.2) would produce melts only in unlikely circumstances, for a very stiff upper mantle and a very fertile lower crust. In the Tangtse area, it has been proposed that Miocene magmatism could result from high heat flow caused by crustal thickening [e.g., *Huerta, et al.*, 1998] and / or heat advection following slab breakoff [*Mahéo, et al.*, 2009]. Melting was probably enhanced by fluid circulation [*Reichardt, et al.*, 2010]. [*Leech*, 2008] even proposed that the KSZ acted as a barrier collecting all magmas flowing at mid-crustal level from North Tibet towards the south in the framework of the lower crustal channel flow model. This hypothesis would explain why Himalayan granites are scarcer and older west of the Gurla Mandata, which is interpreted as the SE tip of the KFZ (Fig. 1b). This hypothesis appears to be sustained by the fact that the South Tibet detachment system (STDS), interpreted as the upper bound of the channel, stopped earlier west of the Gurla Mandata than further east. However, this stop occurred at ca. 17 Ma [*Leloup, et al.*, 2010], ca. 8 Ma after the initiation of magmatism in the KSZ (North Ayilari; NA Fig. 12) [*Valli, et al.*, 2008], and it is therefore difficult to link the two events.

Whatever was the mechanism for magma generation, the KSZ was a good pathway for magma produced deeper in crust. Many magmatic rocks have been dated along the KFZ. We collected 74 published U/Pb ages measured in four different sites: Baltoro granite zone (Pakistan, B Fig. 1b), the Nubra valley (P & C, Fig. 1b), the Tangtse area (India, T Fig. 1b) and the North Ayilari Range area (NA, Fig. 1b) (see Appendix F). When plotted in an age frequency diagram (Fig. 13a) the ages show four major peaks: (1) Upper Lower Cretaceous (106-100 Ma), (2) Upper Cretaceous (76-60 Ma), (3) Oligocene (36-32 Ma) and (4) Miocene (25-12 Ma). Such diagram has no statistical meaning as the database is still too small and depends heavily on the sampling and dating strategy of the authors, however it can be used to evidence the main magmatic events. The two oldest peaks date the formation of the Karakorum (110-75 Ma) and the Kohistan-Ladakh Transhimalayan batholith (70-45 Ma) magmatic arcs (see section 2). Corresponding ages comes from magmatic rocks that have not been remelted in the KSZ (e.g. LA48), or from inherited grains within the Miocene melts (e.g. LA33). The Oligocene magmatic event that was suggested to be possibly linked with the KSZ [*Lacassin, et al.*, 2004; *Rolland, et al.*, 2009] appears limited to the Ayilari range and is thus probably not linked with the onset of the fault.

On the other hand, Lower Miocene magmas are found in most localities where the KSZ has been exhumed and preserved. These Miocene ages show three main peaks at ~15.5 Ma (4c), ~18.5 Ma (4b), and ~22.0 Ma (4a, Fig. 13b). The youngest peak mostly corresponds to leucocratic and pegmatitic dykes, while the two other mostly correspond to larger plutons, migmatites and gneisses. Abundance of pegmatitic and aplitic dykes in the youngest group signs the end of the regional magmatism because leucocratic and pegmatites melts are often extreme differentiation or re-melting and hydrothermal products, which often characterize the end of a magmatic event. This can be correlated to the decrease of the apparent geothermal gradient (fig. 11f) and the return to a "regular" geotherm at ca. 10-12 Ma.

6.2. Long-term kinematics of the KFZ

As mentioned in section 2, correlations of geological units across the KFZ are not well established, and the total offset has been debated, with estimates ranging from no offset [*Jain and Singh*, 2008] to 1000 km [*Peltzer and Tapponnier*, 1988]. This problem is discussed in detail by [*Valli, et al.*, 2008], which deduced from the geometry of the main suture zones an offset of 200 to 240 km in the central part of the fault zone (Between B and SA, Fig. 1b, Table 4). In the same section of the fault *Searle, et al.* [1998] proposed a smaller offset of 120-150 km by correlating the Baltoro granite and the Tangtse mylonitic orthogneiss (Fig. 1b). However, such offset is a minimum bound, as the Tangtse mylonitic orthogneiss is located within the shear zone, and not across it (Fig. 2a). Furthermore with an age of ~15.5 Ma (see section 4.1) the Tangtse mylonitic orthogneiss (LA33) is younger than the onset of

KSZ and thus cannot have registered the full offset. The 120 km offset of the Indus River across the fault [*Gaudemer, et al.*, 1989] (Fig. 2a) is also most likely a minimum offset, for which *Valli, et al.* [2007] proposed an age of 14 ±2 Ma corresponding to the entrenching of the river in the Ayilari range. In the north-western section of the KFZ, *Robinson* [2009b] proposed an offset of 149 to 167 km based on the mapping from satellite image interpretation of the Late Triassic-Early Jurassic Aghil carbonate formation (Fig. 1b). In the same segment of the fault, *Valli, et al.* [2008] proposed a larger offset of 435 to 565 km based on the matching of the Tanymas with the Jinsha sutures and of the Rushan-Pshart with the Bangong suture (Fig. 1b). Across the southeastern section of the KFZ, *Murphy, et al.* [2000] suggested that the South Kailash thrust (SKT on Fig. 1b and 12) was offset by 66 ± 5.5 km.

As discussed above, the present study supports the view that deformation initiated prior to 18.8±0.4 Ma in the Tangtse area, and a comparable study concluded it initiated prior to 22.7±0.1 Ma in the North Ayilari range [*Valli, et al.*, 2008]. This suggests that the Ayilari Range may have been the locus of onset of the KFZ. If the oldest age of the syntectonic granitoids are taken as the timing of onset of deformation, it would imply a propagation rate of the fault of ~50 mm/yr between the North Ayilari (22.7 Ma) and Tangtse (18.8 Ma) (scenario 1a, Fig. 12), and an integrated fault rate of 9.7 to 13 mm/yr for a 200 to 240 km offset (Table 4). On the other hand, if these ages are only considered as minimum ages for deformation, and if the older Miocene magmatism ~25 Ma old in the North Ayilari zone [*Valli, et al.*, 2008], and 21±0.5 Ma for the Baltoro granite [*Parrish and Tirrul*, 1989; *Schärer, et al.*, 1990] are interpreted to coincide with the fault onset, it would imply a propagation rate of the Fault of ~120 mm/yr from the North Ayilari towards the NW (scenario 2a, Fig. 12), and an integrated fault rate of 8.4 to 10.4 mm/yr (Table 4). The proposed ~150 km offset of the Baltoro-Tangtse granites would correspond to a slip rate between 7.7 and 9.7 mm/yr since 15.5 Ma (Table 4). The Indus river offset implies a rate of

7.5 to 10 mm/yr if the entrenching of the river is dated at 14±2 Ma (Table 4) [*Valli, et al.*, 2007].

There are few data to constrain the age of the south-eastern section of the KFZ. A single K-feldspar Ar/Ar thermal history in the footwall of the Kailash thrust suggests a reheating between ~19 and ~13 Ma, interpreted as resulting from the thrust activity [*Yin, et al.*, 1999]. If the Kailash thrust was active between 19 and 13 Ma, and if it was a part of a larger SKT system predating the initiation of the KFZ [e.g., *Murphy, et al.*, 2000], this would constrain the KFZ to be younger than 13 Ma SE of the South Ayilari. This would imply a KFZ slip rate between 3.2 and 5.5 mm/year (Table 4), a dramatic decrease of fault offset towards the SE, and a very slow propagation (≤11 mm/yr, scenario 1b, Fig. 12). However, the age of the Kailash thrust is not well constrained and it could be part of a flower structure linked to the KFZ [*Lacassin, et al.*, 2004]. Alternatively the emplacement of the 21.1±0.3 Ma-old Labhar Kangri granite has been interpreted to be linked with the KFZ [*Valli, et al.*, 2008]. In this case, the southeastward propagation of the fault would have been very rapid (95 mm/yr, scenario 2b, Fig. 12).

On the northern section of the KFZ the offset values vary widely upon authors, and neither the age of onset of the KFZ nor the amount of possible Pre-Miocene offsets are well constrained. Assuming an onset age of ~20 Ma (Fig. 12) would imply rates between 21.7 and 28.2 mm/yr for the larger offset, or between 7.5 and 8.4 mm/yr for the smaller ones (Table 4).

All these rates have been calculated assuming that the fault is still active today, as strongly suggested by evidence for continuous deformation from high until low temperatures (see section 5.2.3), the well-defined morphological trace of the fault, and offset of Quaternary moraines [e.g., *Chevalier, et al.*, 2005; *Chevalier, et al.*, 2012]. If the KFZ is now inactive, as proposed by Wright et al. [2004] for the whole fault, or by Robinson [2009a] for its northern portion, the Miocene rates would have to be significantly increased.

We conclude that the central segment of the KF initiated in the North Ayilari before ~22 Ma ago and propagated towards the NW at high rates of 50 to 120 mm/yr. The fault dextral displacement was on the order of 7.5 to 13 mm/yr. Propagation and fault rates in the northern and southern portions of the fault are not well defined, and await more structural and geochronologic constrains.

6.3. Localization of deformation through time in the Karakorum shear zone.

The Tangtse-Muglib and the Darbuk sections provide the opportunity to determine if the ductile deformation stays localized in the same strand(s) or migrates across strike through time. Further south only a fraction of the shear zone as been preserved in the North Ayilari range, the north-eastern part being down-cut by the active right-lateral / normal Karakorum fault [e.g., *Valli, et al.*, 2008]. In the South Ayilari range, the KSZ has been almost totally removed by normal faulting in the Gar and Baer pull-appart basins [e.g., *Valli, et al.*, 2008].

From the analysis of the relationships between magma emplacement and deformation, it appears that deformation was active coevally in the Muglib and Tangtse strands at least between ~18 and ~15.5 Ma (Fig. 8). However, at the outcrop scale, while undeformed dykes crosscut deformed zones, they are in turn ductily deformed along their length (Fig 6. f and g), indicating that ductile deformation was going on after dyke intrusion few meters away from the zone that had ceased to deform. This indicates that deformation migrated through time within the broad deformation zone (see section 5.1.3). After the granites emplacement, the cooling histories paired with the structural observations (see section 5.3), suggest that ductile deformation was still active everywhere in the 8 km-width shear zone before ~15 Ma (Fig. 8 and 11). The absence of brittle deformation (≤300°C) in the South Tangtse granite suggests that deformation stopped there at ~15 Ma (Fig. 11a, e). Similarly the absence of low temperature deformation (≤200°C) suggests that it stopped at ~7 Ma in the Tangtse strand

(Fig. 11b, e). On the contrary deformation lasted until today in the Muglib strand, where low temperature deformation (≤200°) is attested by the occurrence of brittle structures [e.g., *Rutter, et al.*, 2007], and by an active fault strand that offsets the Quaternary morphology [*Brown, et al.*, 2002]. This suggests that deformation, initially affecting the whole shear zone, progressively concentrated north-eastern wards until to be localized on a single fault today.

During the granites emplacement, the most likely mechanisms for deformation localisation and migration are the presence rheological heterogeneities corresponding to the various rock-facies, and the emplacement of hot plutons that disrupt the temperature field, thus creating other rheological heterogeneities. At lower temperatures the most likely mechanism for strain localisation is the progressive decrease in temperature linked with the vertical component of the strike-slip shear zone. Progressive localization of deformation in ductile shear zones has been observed in other contexts, such as normal faults where it has been related to the temperature decrease. For example *Gueydan, et al.* [2005] estimated that below ~375°C, penetrative deformation localized along small-scale shear bands, and that below ~300°C brittle deformation begins along discrete fault planes.

7. Conclusions

Our reinvestigation of the structure and our 39 new geochronologic ages in the Karakorum shear zone in the Tangtse - Darbuk area lead us to conclude. 1) Right-lateral deformation and most of the Miocene magmatism have been coeval. 2) Ductile deformation started prior to 18.8 ±0.4 Ma. 3) During synkinematic magmatism ductile deformation a) was mostly absorbed in the Tangtse and Muglib mylonitic strands, and b) migrated within the Tangtse strand. 4) Deformation pursued during the exhumation / cooling of the shear zone and progressively migrated across strike from SW to NE, where the active strand of the fault stands. Ductile deformation on the rocks that outcrop now is over since ~8Ma.

When integrated with other published data from all locations along the Karakorum Fault zone, our data suggest. 1) The KFZ has played an important role in the creation and /or collection of crustal melts. 2) The fault zone initiated in the North Ayilari range prior to 22.7 ±0.1 Ma, and propagated quickly to the NW at a rate 5 to 12 cm/yr. 3) Long-term fault rate of the central KFZ integrated to present day is 0.84 to 1.3 cm/yr, considering a total offset of 200 to 240 km. This corresponds also well to the rates estimated for younger and shorter time ranges of 0.75 to 1 cm/yr deduced from the Indus offset [*Valli, et al.*, 2008], the rate of 1.07 ±0.07 mm/yr deduced from the offset of Quaternary moraines [*Chevalier*, *et al.*, 2005] and the present day 1.1 ±0.4 cm/yr GPS rate of [*Banerjee and Bürgmann*, 2002]. It is however significantly different from the 4 ±1 mm/yr rate deduced from the offset of a single debris flow levee [*Brown, et al.*, 2002] and the present day fault rates of 0.34±0.5 cm/yr (GPS) [*Jade, et al.*, 2004]) and 0.1 ±0.3 cm/yr (InSaR) [*Wright, et al.*, 2004]). 4) Propagation to the South and rate of the southern KFZ were possibly much lower but this conclusion awaits for more precise data. 5) The KFZ stayed localized for more than 20 Ma, with a slip rate over 8 mm/yr, showing that large strike-slip discontinuities may be stable at the time-scale of orogeny even when located in areas with high thermal gradient. 5) Source for the synkinematic magmatism is not clearly established but the timing makes it unlikely to be the lower crustal channel flow.

Acknowledgements :

The analytical work was funded by the CNRS⁄ INSU 3F program. Organizers of and participants in the 23rd HKT field excursion in Tangtse are thanked for stimulating discussions on the syntectonic, or not, nature of the granitoids within the KSZ. B. Heulin of the French embassy in New Delhi is thanked for his help in sending back the samples. R. Weinberg is thanked for his detailed and constructive review together with one anonymous reviewer. The Géosciences Montpellier team is thanked for its help with the EBSD, as well as G. Mahéo for discussions on the geology of the Karakorum.

Figures captions:

Figure 1: The Karakorum fault zone in the frame of the India - Eurasia collision.

a) Simplified structural map of the India-Eurasia collision zone. Red frame locates b). **b)** Map of the Karakorum Fault zone. SA, South Ayilari (Namru); NA, North Ayilari; T, Tangtse; D, Darbuk; S, Satti; P, Panamik; Za, Zanskar; TG, Tash Gurgan; Gw, Garwal; GM, Gurla Mandata; LP, Leo Pargil; TM, Tso Morari unit; SKT, South Kailash thrust; NP, Nanga Parbat. Red-framed area corresponds to Fig. 2a. Geological units drawn from bibliography and Landsat imagery interpretation. MKT: Main Karakorum thrust corresponding to the Shyok suture zone ; MMT: Main Mantle Thrust corresponding to the Indus suture zone. From *Leloup, et al.* [2011] modified.

Figure 2: Structure of the KFZ in Tangtse-Darbuk zone.

Most samples discussed in text are located either on a) a map or b) a section. Samples from the South Tangtse granite and Tangste strand near the Tangtse monastery are located on Fig. 5. **a)** Structural map drawn from field observation, satellite image interpretation, and bibliography [*Phillips, et al.*, 2004; *Reichardt, et al.*, 2010; *Rolland, et al.*, 2009; *Weinberg, et al.*, 2009]. UTM 44 projection, the black-framed zone corresponds to Fig. 5a. Plots of foliations and lineations in the various units are Schmidt diagram, lower hemisphere projection. **b)** Cross section along the Tangtse gorge.

Figure 3: U/Pb datations plots and examples of spots location on cathodoluminescence (CL) images.

All plots are Tera-Wasserburg (TW) unless, concordia plots in c) and e); and 207-corrected age vs. U-content plot in j). Samples: a) LA25; b) LA28; c) LA29; d) LA33; e) LA34; f) LA18; g) LA12; h) LA23; i) LA14; j) LA17; k) LA48; l) LA58. In each case, examples of plot locations with corresponding $^{206}Pb/^{238}U$ ages are shown on cathodoluminesence images. The mean Th/U value for zircons rims is indicated. Results are summarized in Table 2 and detailed in Appendix D and E.

Figure 4: Ar/Ar dating.

Results are summarized in Table 3. The age spectra and/or the inverse isochron plots are given. When the plateau age is significant, it is retained and otherwise, the inverse isochron age is retained. In age spectra plots, steps taken into account for the plateau age calculations are designated by a double arrow. In the inverse isochron plots steps taken in the regression calculation are in grey. a) to d) amphiboles; e) to j) muscovites; k) to x) biotites. Samples: a) LA23; b) LA38; c) LA52; d) LA15; e) LA33; f) LA47; g) LA58; h) LA13; i) LA14; j) LA18; k) LA14; l) LA18; m) LA21; n) LA28; o) LA38; p) LA33; q) LA34; r) LA47; s) LA48; t) LA52; u) LA58; v) LA25; w) LA12; x) LA13.

Figure 5: Map of the KSZ near the Tangtse monastery and corresponding cross-section.

a) Structural map corresponding to the black-framed zone on Fig. 2a. Drawn from field observations. UTM projection (zone 44), WGS 84 ellipsoid. Samples are located, with corresponding U/Pb ages when available [*Jain and Singh*, 2008; *Leloup, et al.*, 2011; *Phillips, et al.*, 2004, this study]. The inset is a Schmidt plot of the stretching lineations (lower hemisphere projection). The white black dashed line corresponds to the cross-section seen in b). **b)** Cross section of the Tangtse Gompa area with samples locations. Same legend as for a).

Figure 6: Examples of macroscale relationships between magmatism and deformation in the KSZ near Tangtse.

a) Strongly foliated aplitic dyke LA25, (see also Fig. 7g) transposed parallel to the host gneiss foliation, view from above. **b)** Aplitic dyke LA28, cross-cutting the host gneiss foliation (Foliation N130 72SE lineation pitch 10 W), but itself stretched (see also Fig. 7d), view from above. **c)** Undeformed pegmatitic dyke LA17 (see also Fig. 7a), showing an intrusive contact within the host gneiss (Foliation N170 67W lineation pitch 40 N). West to the right. **d)** Aplitic dyke LA14 stretched parallel to the foliation (see also Fig.7f) in the embedding gneiss LA12 (foliation N145 82SE lineation pitch 37 N). SE to the right. **e)** Network of leucocratic dikes. Most dikes are deformed but some are not and crosscut the foliation. NE to the right. **f)** Leucocratic dike P8 [*Phillips, et al.*, 2004] that crosscuts the ~N130 trending foliation, but exhibits two asymmetric tails indicative of NW-SE ductile right-lateral shear. The intrusive contact is underlined by red short dashes and the foliation by yellow long dashes. Oblique view from above (monastery promontory). **g)** Detail of one of the ductile tails of P8 showing crosscutting (intrusive, red short dashes) relationship with the amphibolitic schists, and concordant contact with the marbles lying parallel to the main shearing direction. Foliation is underlined by yellow long dashes. View from above. **h)** Pegmatitic dyke LA58, stretched and boudinated parallel to the schists foliation (N135 vertical, lineation pitch of 5 SE). The black frame corresponds to i). **i)** Detail of LA58, showing the schist levels embedded in the pegmatite as well as the right-lateral deformation (red arrows). Top: field picture taken from above. Bottom: interpretative sketch. a) and b) from the NE margin of the South Tangtse granite; c, d and e from darbuk section; f and g from the Tangtse strand; h and e from the muglib strand. Samples are located on figures 2 and 5.

Figure 7: Microscale deformation characteristics of the KSZ dykes.

See Figures 2a and 5 for localization and Figure 6 for macroscopic description. **a)** Undeformed pegmatitic dyke LA17 (14.7 ±0.3 Ma) showing large muscovite, feldspar and quartz grains. **b)** Pegmatitic dyke LA60 (16.0 ±0.6 Ma) cross-cutting the schist foliation [*Leloup, et al.*, 2011] showing faint magmatic foliation parallel to the dykes borders, underlined by K-feldspar and quartz, and unrelated to the KSZ deformation. **c)** Pegmatitic dyke LA58 (15.4 ±0.4 Ma), showing large undeformed muscovite, feldspar and quartz grains. This dyke is deformed (boudinated) at a macroscopic scale (Fig. 6h & i). **d)** Aplitic dyke LA28 (18.8 ±0.4 Ma), showing a foliation underlined by quartz, feldspar layers and biotites. As this dyke also cross-cuts the host rock foliation (Fig. 6b), it is interpreted as synkinematic. **e)** Slightly deformed pegmatitic dyke LA13 (14.2 ±0.1 Ma) showing heterogeneous quartz recrystallization and myrmekites in high stress sites. **f)** Slightly deformed aplitic dyke LA14 (14.8 ±0.2 Ma), showing recrystallized quartz and feldspar layers and feldspar porphyroclasts. **g)** Strongly deformed dyke P11 (15.7 ±0.5 Ma) [*Phillips, et al.*, 2004] parallel to the ~N130 trending foliation, and showing C/S fabric. Original picture from *Phillips, et al* [2004]. **h)** Aplitic transposed dyke LA25 (72.3 ±5.0 Ma) (Fig. 6a), with a strong foliation of mica and recrystallized quartz and feldspar. Abbreviations: Qtz = Quartz; Feldsp = feldspar; Bt = Biotite; Ms = muscovite; Chl = chlorite; Gt = Garnet; Recryst. = recrystallized.

Figure 8: Summary of ages and relationships with strike-slip shearing of the magmatic rocks in the Tangtse area.

Samples are presented from SW to the NE (left to right). All ages are for zircons, unless stated with the sample name (Zr: zircon; Ti: titanite; Mz: monazite). Numbers in bracket are key to original references: (1) This study; (2) *Reichardt, et al.* [2010]; (3) *Phillips* [2004]; (4) *Jain and Singh* [2008]; (5) *Phillips, et al.* [2004]; (6) *Searle, et al.* [1998]; (7) *Leloup, et al.* [2011]; (8) *Ravikant, et al.* [2009]. U/Pb Magmatic bodies (granites and dykes) emplaced continuously between at least ~21.6 Ma (LA12) [this study] and ~13.7 Ma (P8), [*Phillips, et al.*, 2004], with no visible trend in age from SW to NE. The oldest and the youngest intrusion with structural evidence for synkinematic emplacement define the minimum fields for right-lateral ductile deformation (grey), see .sections 5.1.2 and 5.1.3 for details.

Figure 9: Microstructures of magmatic bodies in the KSZ near Tangtse.
a) Sample LA33, showing a typical core and mantle structure of quartz – feldspar aggregate recrystallization during right-lateral shear. Left: photomicrograph (plane-polarized light). Right: interpretative drawing. The samples **b)** LA33, **c)** LA34, **d)** LA12 and **e)** LA18 show lower-temperature microstructures of deformation, such as myrmekites, bent twin lamellae and sealed microfractures. **f)** Sample LA29, showing alternation of recrystallized quartz and feldspar layers. These five samples display indicators of synkinematic cooling from high temperatures (T>500°C, core and mantle structure for quartz-feldspar aggregates), to low temperature (T<300°C, sealed microfractures) during right-lateral shear. **g)** Sample LA48 showing no visible deformation. See Figures 2a and 5 for localization.

Figure 10: Example of recrystallized quartz ribbons within the KSZ.
For each sample: left cross-polarized micrography, centre: interpretation drawing of grain boundaries, up right: Lattice Preferred Orientation of quartz crystals, down right: Crystal Shape Orientation (long axis of the best approximated ellipse). **a)** Sample LA26 (sampled close to LA25 and LA28, Fig. 5) shows large grains with lobbed shapes (GBM), and small grains recrystallized by SGR. The <c>-axis quartz fabric indicates the activation of the prismatic-<a> slip system. **b)** LA30 (sampled close to LA33, Fig. 5) shows small geometric grains recrystallized by SGR. The <c>-axis quartz fabric indicates the preferential activation of the prismatic-<a> slip system. **c)** LA59 (sampled close to LA58, Fig. 2b) shows large

grains with lobbed shapes (GBM). The <c>-axis quartz fabric indicates the activation of the prismatic-<a> slip system.

Figure 11: Cooling history of the KSZ in the Tangtse - Darbuk area.

a) South Tangtse granite, **b)** Tangtse strand; **c)** Pangong range and **d)** Muglib strand. Data are from this study (Table 2) and from the bibliography (Appendix F). The name of samples cited in section 4.2 are given. Closure temperatures are given in sections 3.2 and 3.3. The zircon U/Pb closure temperature for dikes has been artificially lowered by 50°C to reflect the fact that the dikes may have emplaced in cooler country rocks. K-feldspar models are from *Dunlap, et al* [1998]]. Temperature ranges for which there is structural evidence for cooling coeval with right-lateral deformation are reported. See section 5.2 and e) for details. **e)** microstructural indicators for deformation temperatures in each structural unit. **f)** P-T-t path of the Pangong Range, drawn from P-T that of *Rolland, et al.* [2009] and the T-t path shown in c). Estimations of the apparent local geothermal gradients at each time period are shown in blue frames.

Figure 12: Age constraints on the onset and propagation of the KFZ.

U/Pb ages are plotted along the strike of the fault. Green diamonds indicate syntectonic granitoids [*Leloup, et al.*, 2011; *Reichardt, et al.*, 2010 this study; *Valli, et al.*, 2008; *Wang, et al.*, 2011]. Data and corresponding references are reported in Appendix F. K, Kailas; NA, North Ayilari; SA, South Ayilari; T, Tangtse; D, Darbuk; S, Satti; P, Panamik; B, Baltoro; GM, Gurla Mandata; SKT, South Kailas Thrust. The green line delineates the minimum age for the KFZ initiation (scenario 1a), assuming that the oldest synkinematic granitoids (green framed diamonds) date the fault initiation. The red line delineates the maximum age for the KFZ initiation (scenario 2), assuming all Miocene granitoids (blue diamonds) are synkinematic. The dashed green line delineates the KFZ propagation to the SE if the SKT was active until ~13 Ma and if it predates the KFZ (scenario 1b). In each case, the corresponding fault propagation rates (FPR) are indicated below the line. See section 6.2 for details. The blue line delineates the timing of South Tibetan detachment system (STDS) end of motion, according to *Leloup, et al.* [2010]. Modified from *Leloup, et al* [2011].

Figure 13: Population histogram of published U/Pb ages along the KFZ

a) Mesozoic and Cenozoic ages, 74 data. Paleozoic and Precambrian inherited ages have not been plotted. See Appendix F for the references. Four main magmatic events are distinguished (1, 2, 3 and 4, see section 6.1). **b)** Neogene granitoids, 48 Data. Three main magmatic events are distinguished within event 4 (4a, 4b and 4c). See section 6.1 for details.

Tables captions

Table 1: Sample characteristics and location

Table 2: U/Pb ages

Table 3 : Ar/Ar ages.

Table 4 : KFZ offsets, onset ages and corresponding fault rates

References :

Avouac, J. P., and P. Tapponnier (1993), Kinematic model of active deformation in central Asia, *Geophys. Res. Lett.*, *20*, 895-898.

Banerjee, P., and R. Bürgmann (2002), Convergence across the northwest Himalaya from GPS measurements, *Geophys. Res. Lett.*, *29*.

Brown, E., et al. (2002), Slip rates of the Karakoram fault, Ladakh, India, determined using cosmic ray exposure dating of debris flows and moraines, *J. Geophys. Res.*, *107*.

Chevalier, M.-L., et al. (2005), Slip-Rate measurements on the Karakorum Fault may imply secular variations in fault motion, *Science*, *307*, 411-414.

Chevalier, M.-L., et al. (2012), Spatially constant slip rate along the southern segment of the Karakorum fault since 200 ka, *Tectonophysics*, *530-531*, 152–179.

Clemens, J. D. (2003), S-type granitic magmaspetrogenetic issues, models, and evidence, *Earth Sc. Rev.*, *61*, 1-18.

Clift, P. D., et al. (2002), Constraints on India–Eurasia collision in the Arabian Sea region taken from the Indus Group, Ladakh Himalaya, India, in *The Tectonic and Climatic Evolution of the Arabian Sea Region*, edited by P. D. Clift, Kroon, D., Gaedicke, C., Craig, J., pp. 97-116, Geological Society, London.

Deves, M., et al. (2011), Localised and distributed deformation in the lithosphere: modelling the Dead Sea region in 3 dimensions, *Earth Planet. Sci. Lett.*, *308*, 172-184.

Dunlap, W., et al. (1998), Karakorum fault zone rocks cool in two phases, *J. Geol. Soc. London*, *155*, 903-912.

Dunlap, W. J., and R. Wysoczanski (2002), Thermal evidence for early Cretaceous metamorphism in the Shyok suture zone and age of the Khardung Volcanic rocks, Ladakh, India, *J. Asian Earth Sci.*, *20*, 481-490.

Ehiro, M., et al. (2007), Discovery of Jurassic ammonoids from the Shyok suture zone to the northeast of Chang La Pass, Ladakh, northwest India and its tectonic significance, *Island Arc*, *16*, 124-132.

England, P., et al. (1985), Length scales for continental deformation in convergent, divergent and strike-slip environments, analytical and approximate solutions for a thin viscous sheet model, *J. Geophys. Res.*, *90*, 3551-3557.

England, P., and D. McKenzie (1982), A thin viscous sheet model for continental deformation, *Geophys. J. R. Astron. Soc.*, *70*, 295-321.

Gapais, D. (1989), Shear structures within deformed granites: mechanical and thermal indications, *Geology*, *17*, 1144-1147.

Gapais, D., and B. Barbarin (1986), Quartz fabric transition in a cooling syntectonic granite (Hermitage massif, France), *Tectonophysics*, *125*, 357-370.

Gates, A. E., and L. Glover (1989), Alleghanian tectono-thermal evolution of the dextral transcurrent Hylas zone, Virginia Piedmont, USA, *J. Struct. Geol.*, *11*, 407-419.

Gaudemer, Y., et al. (1989), River offsets across active strike-slip faults, *Ann. Tectonicae*, *3*, 55–76.

Gower, J. W., and C. Simpson (1992), Phase boundary mobility in naturally deformed, high-grade quartzofeldspathic rocks: Evidence for diffusional creep, *J. Struct. Geol.*, *14*, 301-313.

Gueydan, F., et al. (2005), Stress- strain rate history of a midcrustal shear zone and the onset of brittle deformation inferred from quartz recristallized grain size, in *Deformation mechanisms, rheology and tectonics : from minerals to the lithosphere* edited by D. Gapais, et al., pp. 127-142, Geological society of London, London.

Guillot, S., et al. (2003), Reconstructing the total shortening history of the NW Himalaya, *Geochem. Geophys. Geosyst*, *4*, 1064.

Hames, W. E., and S. Bowring (1994), An empirical evaluation of the argon diffusion geometry in muscovite, *Earth Planet. Sci. Lett.*, *124*, 161-169.

Harrison, T. M. (1981), Diffusion of 40Ar in hornblende, *Contrib. Mineral. Petrol.*, *78*, 324-331.

Harrison, T. M., et al. (1985), Diffusion of 40Ar in biotite: temperature, pressure and compositional effect, *Geochimica Cosmichimica Acta*, *49*, 2461-2468.

Hasalova, P., et al. (2011), Microstructural evidence for magma confluence and reusage of magma pathways: implications for magma hybridization, Karakoram Shear Zone in NW India, *J. Metamorph. Geol.*

Hirth, G., and J. Tullis (1991), Dislocation creep regimes in quartz aggregates, *J. Struct. Geol.*, *14*, 145-159.

Houseman, G., and P. England (1993), Crustal thickening versus lateral expulsion in the Indian-Asian continental collision, *J. Geophys. Res.*, *98*, 12233-12250.

Huerta, A. D., et al. (1998), The thermal structure of collisional orogens as a response to accretion, erosion, and radiogenic heating, *J. Geophys. Res.*, *103*, 15287–15302.

Hutton, D. H. W., and R. J. Reavy (1992), Strike-slip tectonics and granite petrogenesis, *Tectonics*, *11*, 960–967.

Jade, S., et al. (2004), GPS measurements form the Ladakh Himalaya, India: preliminary tests of plate-like or continuous deformation in Tibet, *Geol. Soc. Am. Bull.*, *116*, 1385-1391.

Jain, A., and S. Singh (2008), Tectonics of the southern Asian Plate margin along the Karakoram Shear Zone: constraints from field observations and U-Pb SHRIMP ages, *Tectonophysics*, *451*, 186-205.

Jensen, L. N., and J. Starkey (1985), Plagioclase microfabrics in a ductile shear zone from the Jotun Nappe, Norway, *J. Struct. Geol.*, *7*, 527-539.

Ji, S., and D. Mainprice (1990), Recrystallization and fabric development in plagioclase, *J. Geol.*, *98*, 65-79.

Lacassin, R., et al. (2004), Large-scale geometry, offset and kinematic evolution of the Karakorum fault, Tibet, *Earth Planet. Sci. Lett.*, *219*, 255-269.

Langille, J. M., et al. (2012), Timing of metamorphism, melting, and exhumation of the Leo Pargil dome, northwest India, *Journal of Metamorphic Geology*, *accepted*

Leech, M. L. (2008), Does the Karakoram fault interrupt mid-crustal channel flow in the western Himalaya?, *Earth Planet. Sci. Lett.*, *276*, 314–322.

Leloup, P. H., et al. (2001), New constraints on the structure, thermochronology and timing of the Ailao Shan - Red River shear zone, SE Asia., *J. Geophys. Res.*, *106*, 6683-6732.

Leloup, P. H., et al. (2011), Long-lasting intracontinental strike-slip faulting: new evidence from the Karakorum shear zone in the Himalayas, *Terra Nova*, *23*, 92-99.

Leloup, P. H., and J. R. Kienast (1993), High-temperature metamorphism in a major strike-slip shear zone: the Ailao Shan–Red River, People's Republic of China, *Earth Planet. Sci. Lett.*, *118*, 213–234.

Leloup, P. H., et al. (1995), The Ailao Shan-Red River shear zone (Yunnan, China), Tertiary transform boundary of Indochina, *Tectonophysics*, *251*, 3-84.

Leloup, P. H., et al. (2010), The South Tibet Detachment shear zone in the Dinggye area. Time constraints on extrusion models of the Himalayas., *Earth Planet. Sci. Lett.*, *292*, 1-16.

Leloup, P. H., et al. (1999), Shear heating in continental strike-slip shear zones: numerical modeling and case studies., *Geophys. J. Int.*, *136*, 19-40.

Mahéo, G., et al. (2009), Partial melting of mantle and crustal sources beneath South Karakorum, Pakistan: implications for the Miocene geodynamic evolution of the India-Asia convergence zone, *J. Petrol.*, *50*, 427-449.

Mainprice, D., et al. (1986), Dominant c-slip in naturally deformed quartz: implications for dramatic plastic softening at high temperature, *Geology*, *14*, 819-822.

Mancktelow, N. S., and G. Pennacchioni (2005), The control of precursor brittle fracture and fluid rock interaction on the development of single and paired ductile shear zones, *J. Struct. Geol.*, *27*, 645-661.

Matte, P., et al. (1996), Tectonics of Western Tibet between the Tarim and the Indus, *Earth Planet. Sci. Lett.*, *142*, 311 - 330.

Mc Carthy, M. R., and R. F. Weinberg (2010), Structural complexity resulting from pervasive ductile deformation in the Karakoram shear zone, Ladakh, NW India, *Tectonics*, *29*.

Molnar, P., and P. England (1990), Temperatures, heat flux, and frictional stress near major thrust faults, *J. Geophys. Res.*, *95*, 4833-4856.

Murphy, M., et al. (2000), Southward propagation of the Karakoram fault system, Southwest Tibet; timing and magnitude of slip, *Geology*, *28*, 451- 454.

Nicolas, A., et al. (1977), Geological aspects of deformation in continental shear zones, *Tectonophysics*, *42*, 55-73.

Olesen, N. O. (1987), Plagioclase fabric development in a high-grade shear zone, Jotunheimen, Norway, *Tectonophysics*, *142*, 291-308.

Olsen, T. S., and D. L. Kohlstedt (1985), Natural deformation and recrystallisation of some intermediate plagioclase feldspars, *Tectonophysics*, *111*, 107-131.

Parrish, R. R., and R. Tirrul (1989), U-Pb age of the Baltoro granite, Northwest Himalaya, and implications for monazite U-Pb systematics, *Geology*, *17*, 1076-1079.

Passchier, C. W., and R. A. J. Trouw (1998), *Microtectonics*, Springer.

Paterson, S. R., and K. L. Schmidt (1999), Is there a close spatial relationship between faults and plutons?, *J. Struct. Geol.*, *21*, 1131-1142.

Pêcher, A., et al. (2008), Stress field evolution in the northwest Himalayan syntaxis, northern Pakistan, *Tectonics*, *27*, .

Peltzer, G., and P. Tapponnier (1988), Formation and evolution of strike-slip faults, rifts, and basins during the India-Asia collision: an experimental approach, *J. Geophys. Res.*, *93*, 15,085 – 015,117.

Pennacchioni, G., and N. S. Mancktelow (2007), Nucleation and initial growth of a shear zone network within compositionally and structurally heterogeneous granitoids under amphibolite facies conditions, *J. Struct. Geol.*, *29*, 1757-1780.

Petterson, M. G., and B. F. Windley (1985), Rb-Sr dating of the Kohistan arc-batholith in the trans Himalaya of north Pakistan, and tectonic implication, *Earth Planet. Sci. Lett.*, *74*, 45-57.

Phillips, R. (2004), Macro- and micro-structural evolution of the Karakoram fault, NW Himalaya, Ph.D. thesis, Oxford.

Phillips, R., et al. (2004), Age constraints on ductile deformation and long-term slip rates along the Karakoram fault zone, Ladakh, *Earth Planet. Sci. Lett.*, *226*, 305-319.

Phillips, R., and M. Searle (2007), Macrostructural and microstructural architecture of the Karakoram fault: relationship between magmatism and strike-slip faulting, *Tectonics*, *26*.

Ratschbacher, L., et al. (1994), Distributed deformation in Southern and Western Tibet as result of the India-Asia collision, *J. Geophys. Res.*, *99*, 19,917 – 919,945.

Ravikant, V., et al. (2009), Zircon U–Pb and Hf isotopic constraints on petrogenesis of the Cretaceous–Tertiary granites in eastern Karakoram and Ladakh, India, *Lithos*, *110*, 153–166.

Reichardt, H., and R. F. Weinberg (2011), The dike swarm of the Karakoram shear zone, Ladakh, NW India: linking granite source to batholith, *Geol. Soc. Am. Bull.*, doi: 10.1130/B30394.1.

Reichardt, H., et al. (2010), Hybridization of granitic magmas in the source: the origin of the Karakoram Batholith, Ladakh, NW India, *Lithos*, *116*, 249-272.

Robinson, A. (2009a), Evidence against Quaternary slip on the northern Karakorum Fault suggests kinematic reorganization at the western end of the Himalayan-Tibetan orogen, *Earth Planet. Sci. Lett.*, *286*, 158-170.

Robinson, A. (2009b), Geologic offsets across the northern Karakorum fault: Implications for its role and terrane correlations in the western Himalayan-Tibetan orogen, *Earth Planet. Sci. Lett.*

Rocchi, S., et al. (2003), Intraplate strike-slip tectonics as an alternative to mantle plume activity for the Cenozoic rift magmatism in the Ross Sea region, Antarctica, *Geological Society, London, Special Publications*, *210*, 145-158

Rolland, Y., et al. (2009), Syn-kinematic emplacement of the Pangong metamorphic and magmatic complex along the Karakorum Fault (N Ladakh), *J. Asian Earth Sci.*, *34*, 10–25.

Rolland, Y., et al. (2000), Middle Cretaceous back-arc formation and arc evolution along the Asian margin: the Shyok Suture Zone in northern Ladakh (NWHimalaya), *Tectonophysics*, *325*, 145-173.

Roy, P., et al. (2010), Microstructures of mylonites along the Karakoram Shear Zone, Tangste Valley, Pangong Mountains, Karakoram, *J. Geol. Soc. India*, *75*, 679-694.

Rubatto, D., et al. (2001), Zircon and monazite response to prograde metamorphism in the Reynolds Range, central Australia, *Contrib. Mineral. Petrol.*, *140*, 458- 468.

Rutter, E. H., et al. (2007), Rock deformation processes in the Karakoram fault zone, Eastern Karakoram, Ladakh, NW India, *J. Struct. Geol.*, *29*, 1315-1326.

Schärer, U., et al. (1990), Age, cooling history and origin of post-collisional leucogranites in the Karakoram batholith; a multisystem isotope study N. Pakistan, *J. Geol.*, *98*, 233-251.

Searle, M. P., and R. J. Phillips (2007), Relationships between right-lateral shear along the Karakoram fault and metamorphism, magmatism, exhumation and uplift: evidence from the K2–Gasherbrum–Pangong ranges, north Pakistan and Ladakh, *J. Geol. Soc. London*, *164*, 439–450.

Searle, M. P., et al. (1998), Transpressional tectonics along the Karakoram fault zone, northern Ladakh: constraints on Tibetan extrusion, in *Continental Transpressional and Transtensional Tectonics*, edited by R. E. Holdsworth, et al., pp. 307-326.

Simpson, C., and R. P. Wintsch (1989), Evidence for deformation-induced K-feldspar replacement by myrmekite, *J. Metamorph. Geol.*, *7*, 261-275.

Stesky, R. M. (1978), Mechanisms of high temperature frictional sliding in Westerly granite, *Can. J. Earth Sci.*, *15*, 361-375.

Stesky, R. M., et al. (1974), Friction in faulted rock at high temperature and pressure, *Tectonophysics*, *23*, 177-203.

Stipp, M., et al. (2002), The eastern Tonale fault zone: a "natural laboratory" for crystal plastic deformation of quartz over a temperature range from 250 to 700 °C, *J. Struct. Geol.*, *24*, 1861-1884.

Stipp, M., et al. (2006), Effect of water on the dislocation creep microstructure and flow stress of quartz and implications for the recrystallized grain size piezometer, *Journ. Geophys. Res.*, *111*.

Streule, M. J., et al. (2009), Evolution and chronology of the Pangong Metamorphic Complex adjacent to the Karakoram Fault, Ladakh: constraints from thermobarometry, metamorphic modelling and U–Pb geochronology, *J. Geol. Soc. London*, *166*, 919–932.

Tapponnier, P., et al. (1986), On the mechanics of the collision between India and Asia, in *Collision Tectonics*, edited by M. P. Coward and A. C. Ries, pp. 115-157, Geological Society, London.

Tapponnier, P., et al. (2001), Oblique stepwise rise and growth of the Tibet plateau, *Science*, *294*, 1671-1677.

Thompson, A. B., and J. A. D. Connolly (1995), Melting of the continental crust; Some thermal and petrological constraints on anatexis in continental collision zones and other tectonic settings, *J. Geophys. Res.*, *100*, 15565-15579.

Tsurumi, J., et al. (2003), Strain localization due to a positive feedback of deformation and myrmekite-forming reaction in granite and aplite mylonites along the Hatagawa shear zone of NE Japan, *J. Struct. Geol.*, *25*, 557-574.

Tullis, J., and R. A. Yund (1987), Transition from cataclastic flow to dislocation creep of feldspar: mechanisms and microstructures, *Geology*, *15*, 606-609.

Upadhyay, R., et al. (2008), Tectonic implications of new U–Pb zircon ages of the Ladakh batholith, Indus suture zone, northwest Himalaya, India, *Terra Nova*, *20*, 309-317.

Valli, F., et al. (2007), 20 million years of continuous deformation along the Karakorum fault, Western Tibet: a thermochronological analysis, *Tectonics*, *26*.

Valli, F., et al. (2008), New U-Th/Pb constraints on timing of shearing and long-term slip-rate on the Karakorum fault, *Tectonics*, *27*.

Wang, S., et al. (2009), New radiometric dating constrains the time for initiation of the Karakorum fault zone (KFZ), SW Tibet, *Tectonophysics*.

Wang, S., et al. (2011), U–Pb SHRIMP and 40Ar/39Ar ages constrain the deformation history of the Karakoram fault zone (KFZ), SW Tibet, *Tectonophysics*, *509*, 208–217.

Weinberg, R., et al. (2000), New field, structural and geochronological data from the Shyok and Nubra valleys, northern Ladakh: Linking Kohistan to Tibet, in *Tectonics of the Nanga Parbat Syntaxis and the Western Himalaya*, edited by A. Khan, Treloar, P.J., and Searle, M.P., pp. 253-275, London.

Weinberg, R. F., and W. J. Dunlap (2000), Growth and deformation of the Ladakh Batholith, Northwest Himalayas: implications for timing of continental collision and origin of calc-alkaline batholiths, *J. Geol.*, *108*, 303-320.

Weinberg, R. F., et al. (2009), Magma ponding in the Karakoram shear zone, Ladakh, NW India, *Geol. Soc. Am. Bull.*, *121*, 278-285.

Weinberg, R. F., and G. Mark (2008), Magma migration, folding, and disaggregation of migmatites in the Karakoram Shear Zone, Ladakh, NW India, *Geol. Soc. Am. Bull.*, *120*, 994–1009.

White, J. C., and C. K. Mawer (1986), Extreme ductility of feldspars from a mylonite, Parry Sound, Canada, *J. Struct. Geol.*, *8*, 133-143.

White, S. (1975), Tectonic deformation and recrystallisation of oligoclase, *Contrib. Mineral. Petrol.*, *50*, 287-304.

Williams, I., et al. (2000), U-Pb dating of Tasmanian dolerites: a cautionary tale of SHRIMP analysis of high-U zircon, paper presented at New frontiers in Isotope Geoscience.

Wright, T., et al. (2004), InSAR observations of low slip rates on the major faults of Western Tibet, *Science*, *305*, 236-239.

Yin, A., et al. (1999), Tertiary deformation history of southeastern and southwestern Tibet during the Indo-Asian collision, *Geol. Soc. Am. Bull.*, *111*, 1644 - 1664.

Zhang, L.-S., and U. Schärer (1999), Age and origin of magmatism along the Cenozoic Red River shear belt, China, *Contrib. Mineral. Petrol.*, *134*, 67-85.

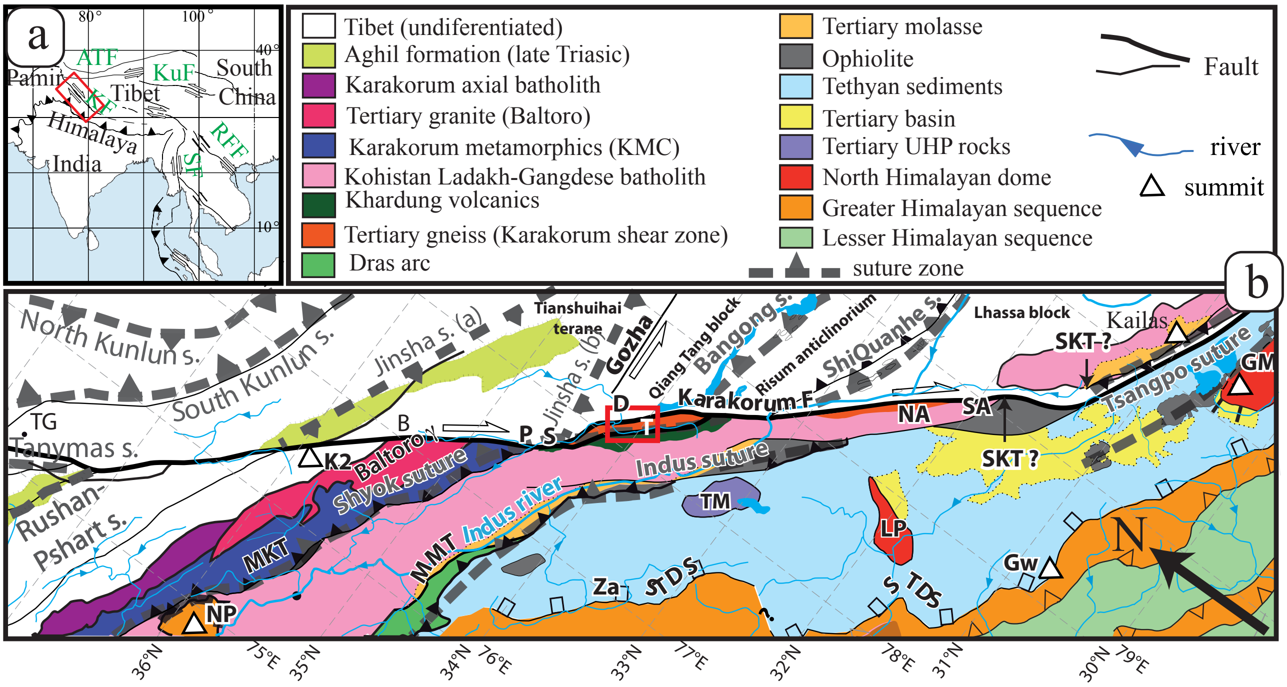
a
ATF
KuF
Pamir
Tibet
South
China
KF
Himalaya
RFF
SF
India
Tibet (undiferentiated)
Aghil formation (late Triasic)
Karakorum axial batholith
Tertiary granite (Baltoro)
Karakorum metamorphics (KMC)
Kohistan Ladakh-Gangdese batholith
Khardung volcanics
Tertiary gneiss (Karakorum shear zone)
Dras arc
Tertiary molasse
Ophiolite
Tethyan sediments
Tertiary basin
Tertiary UHP rocks
North Himalayan dome
Greater Himalayan sequence
Lesser Himalayan sequence
suture zone
Fault
river
summit
b
North Kunlun s.
South Kunlun s.
Jinsha s. (a)
Jinsha s. (b)
Tianshuihai terane
Gozha
Qiang Tang block
Bangong s.
Risum anticlinorium
ShiQuanhe s.
Lhassa block
Kailas
SKT ?
Tsangpo suture
GM
TG
Tanymas s.
Rushan-Pshart s.
K2
B
Baltoro
P
S
D
T
Karakorum F
NA
SA
Shyok suture
Indus suture
Indus river
TM
LP
MKT
MMT
NP
Za
STDS
Gw
N
36°N
75°E
35°N
34°N
76°E
33°N
77°E
32°N
78°E
31°N
30°N
79°E

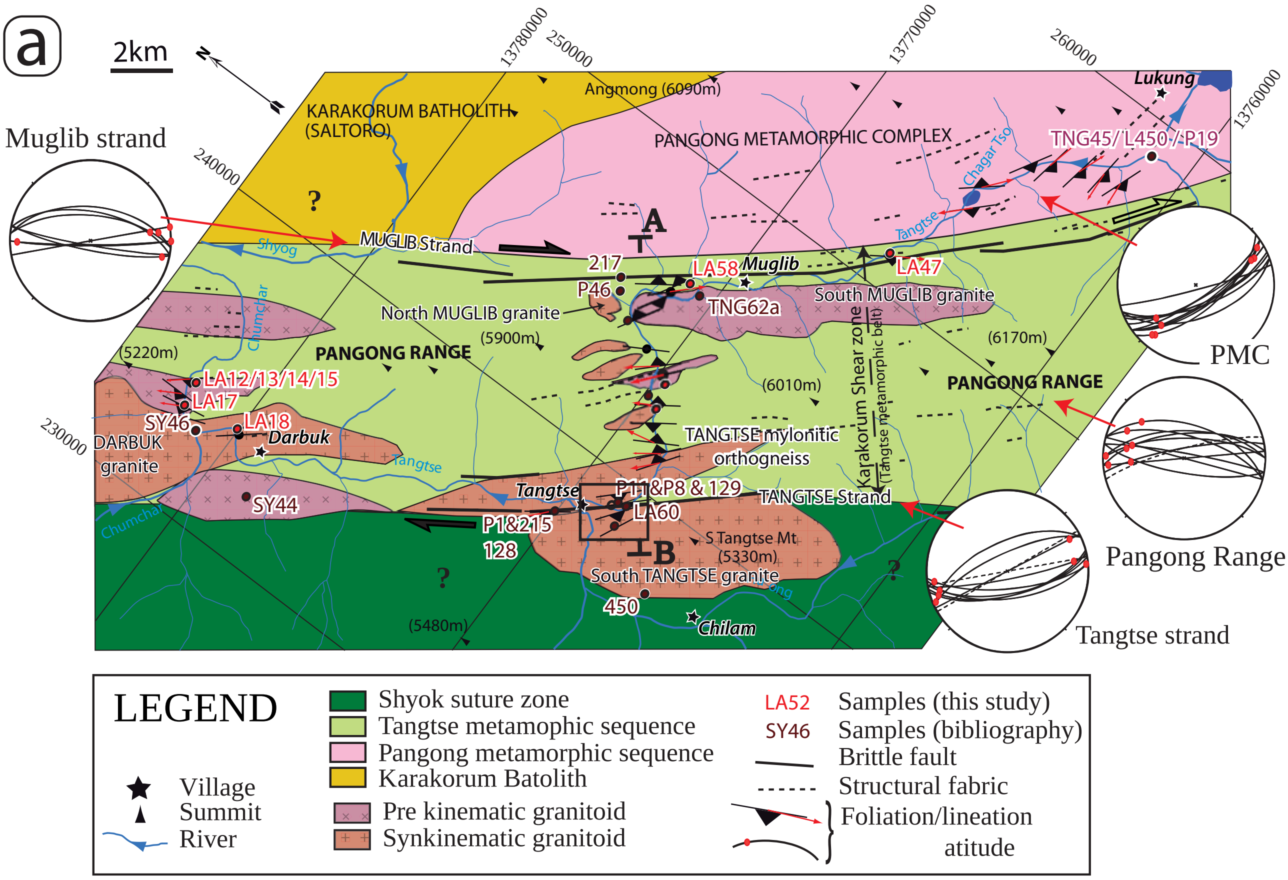
a
2km
N
Muglib strand
PMC
Pangong Range
Tangtse strand
13780000
250000
13770000
260000
13760000
240000
230000
KARAKORUM BATHOLITH
(SALTORO)
Angmong (6090m)
PANGONG METAMORPHIC COMPLEX
Lukung
Chagar Tso
TNG45/ L450 / P19
Tangtse
Shyog
MUGLIB Strand
A
217
P46
LA58
Muglib
LA47
TNG62a
South MUGLIB granite
North MUGLIB granite
(5900m)
(6170m)
(5220m)
PANGONG RANGE
PANGONG RANGE
(6010m)
Karakorum Shear zone
(Tangtse metamorphic belt)
Chumchar
LA12/13/14/15
LA17
SY46
LA18
Darbuk
DARBUK
granite
Tangtse
TANGTSE mylonitic
orthogneiss
SY44
Tangtse
P11&P8 & 129
TANGTSE Strand
LA60
P1&215
128
S Tangtse Mt
(5330m)
B
South TANGTSE granite
450
Chilam
(5480m)
Chumchar
?
?
?
LEGEND
Shyok suture zone
Tangtse metamophic sequence
Pangong metamorphic sequence
Karakorum Batolith
Pre kinematic granitoid
Synkinematic granitoid
Village
Summit
River
LA52 Samples (this study)
SY46 Samples (bibliography)
Brittle fault
Structural fabric
Foliation/lineation
atitude

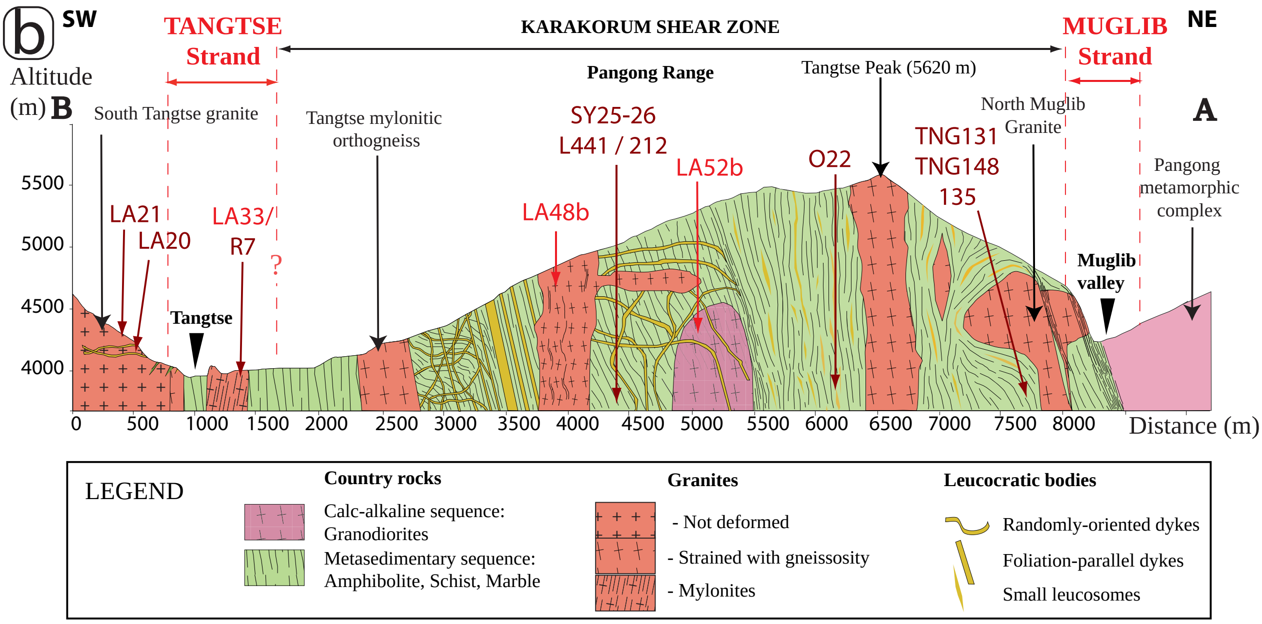

b
SW
NE
TANGTSE Strand
KARAKORUM SHEAR ZONE
MUGLIB Strand
Altitude (m)
B
A
Pangong Range
Tangtse Peak (5620 m)
South Tangtse granite
Tangtse mylonitic orthogneiss
North Muglib Granite
Pangong metamorphic complex
SY25-26
L441 / 212
LA52b
O22
TNG131
TNG148
135
LA21
LA20
LA33/
R7
?
LA48b
Tangtse
Muglib valley
5500
5000
4500
4000
0
500
1000
1500
2000
2500
3000
3500
4000
4500
5000
5500
6000
6500
7000
7500
8000
Distance (m)
LEGEND
Country rocks
Calc-alkaline sequence: Granodiorites
Metasedimentary sequence: Amphibolite, Schist, Marble
Granites
- Not deformed
- Strained with gneissosity
- Mylonites
Leucocratic bodies
Randomly-oriented dykes
Foliation-parallel dykes
Small leucosomes

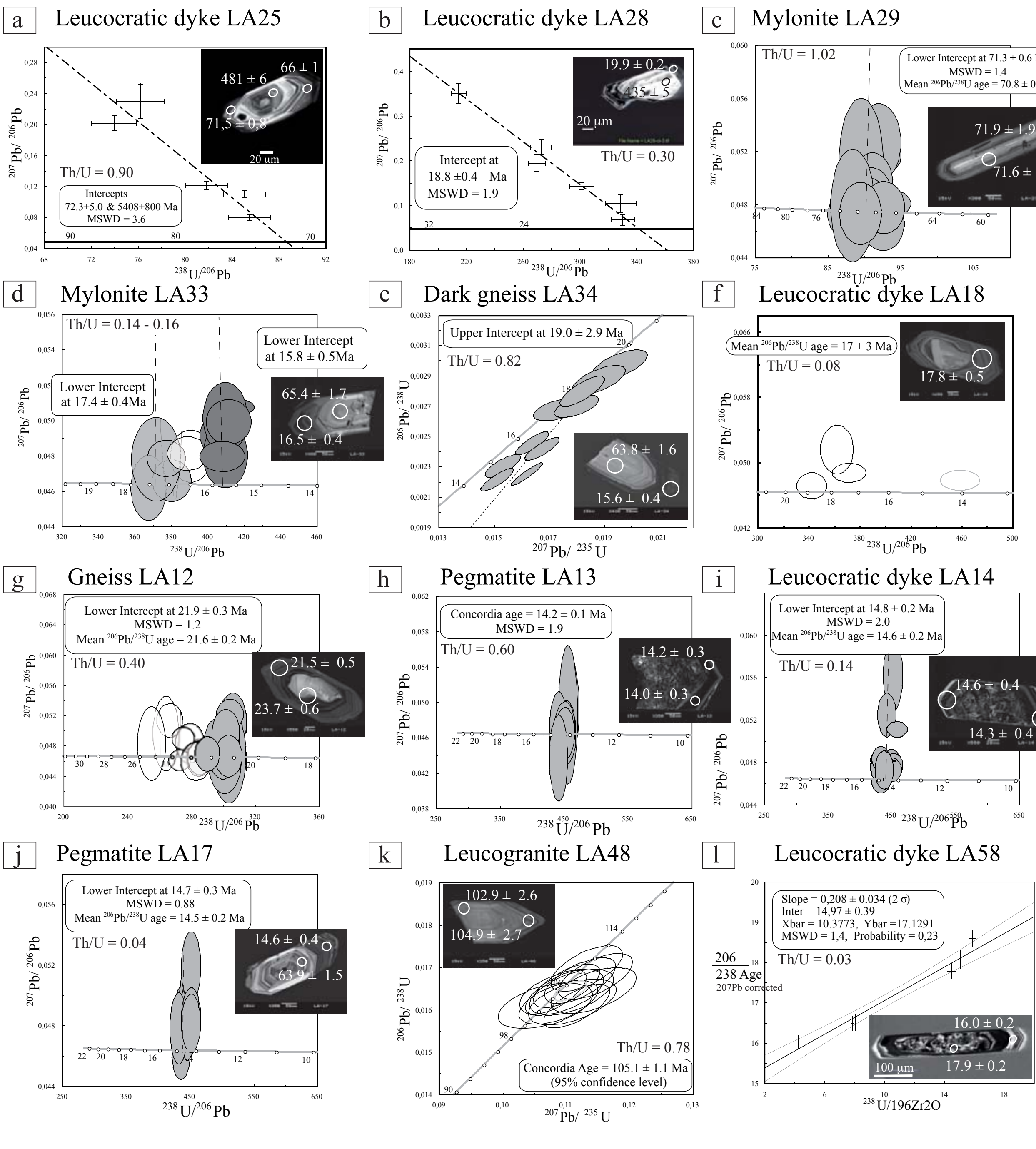
a Leucocratic dyke LA25
481 ± 6
66 ± 1
71,5 ± 0,8
20 µm
Th/U = 0.90
Intercepts
72.3±5.0 & 5408±800 Ma
MSWD = 3.6
b Leucocratic dyke LA28
19.9 ± 0.2
435 ± 5
20 µm
Intercept at
18.8 ±0.4 Ma
MSWD = 1.9
Th/U = 0.30
c Mylonite LA29
Th/U = 1.02
Lower Intercept at 71.3 ± 0.6 Ma
MSWD = 1.4
Mean 206Pb/238U age = 70.8 ± 0.5 Ma
71.9 ± 1.9
71.6 ± 1.9
d Mylonite LA33
Th/U = 0.14 - 0.16
Lower Intercept at 15.8 ± 0.5Ma
Lower Intercept at 17.4 ± 0.4Ma
65.4 ± 1.7
16.5 ± 0.4
e Dark gneiss LA34
Upper Intercept at 19.0 ± 2.9 Ma
Th/U = 0.82
63.8 ± 1.6
15.6 ± 0.4
f Leucocratic dyke LA18
Mean 206Pb/238U age = 17 ± 3 Ma
Th/U = 0.08
17.8 ± 0.5
g Gneiss LA12
Lower Intercept at 21.9 ± 0.3 Ma
MSWD = 1.2
Mean 206Pb/238U age = 21.6 ± 0.2 Ma
Th/U = 0.40
21.5 ± 0.5
23.7 ± 0.6
h Pegmatite LA13
Concordia age = 14.2 ± 0.1 Ma
MSWD = 1.9
Th/U = 0.60
14.2 ± 0.3
14.0 ± 0.3
i Leucocratic dyke LA14
Lower Intercept at 14.8 ± 0.2 Ma
MSWD = 2.0
Mean 206Pb/238U age = 14.6 ± 0.2 Ma
Th/U = 0.14
14.6 ± 0.4
14.3 ± 0.4
j Pegmatite LA17
Lower Intercept at 14.7 ± 0.3 Ma
MSWD = 0.88
Mean 206Pb/238U age = 14.5 ± 0.2 Ma
Th/U = 0.04
14.6 ± 0.4
63.9 ± 1.5
k Leucogranite LA48
102.9 ± 2.6
104.9 ± 2.7
Th/U = 0.78
Concordia Age = 105.1 ± 1.1 Ma
(95% confidence level)
l Leucocratic dyke LA58
Slope = 0,208 ± 0.034 (2 σ)
Inter = 14,97 ± 0.39
Xbar = 10.3773, Ybar =17.1291
MSWD = 1,4, Probability = 0,23
Th/U = 0.03
206/238 Age
207Pb corrected
16.0 ± 0.2
17.9 ± 0.2
100 µm
238U/196Zr2O
238U/206Pb
207Pb/206Pb
206Pb/238U
207Pb/235U

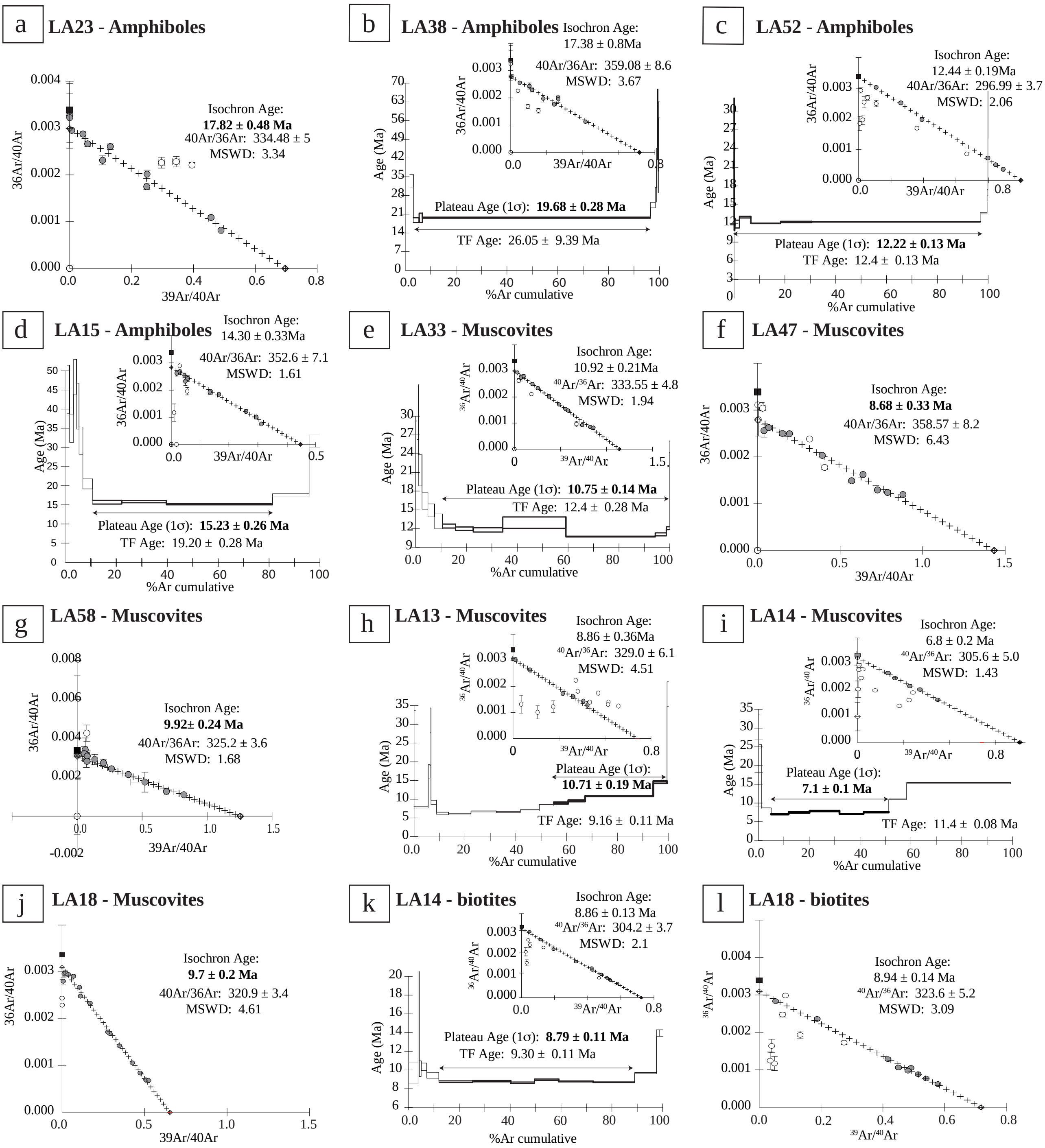

a
LA23 - Amphiboles
Isochron Age:
17.82 ± 0.48 Ma
40Ar/36Ar: 334.48 ± 5
MSWD: 3.34
36Ar/40Ar
39Ar/40Ar
b
LA38 - Amphiboles
Isochron Age:
17.38 ± 0.8Ma
40Ar/36Ar: 359.08 ± 8.6
MSWD: 3.67
36Ar/40Ar
39Ar/40Ar
Age (Ma)
Plateau Age (1σ): 19.68 ± 0.28 Ma
TF Age: 26.05 ± 9.39 Ma
%Ar cumulative
c
LA52 - Amphiboles
Isochron Age:
12.44 ± 0.19Ma
40Ar/36Ar: 296.99 ± 3.7
MSWD: 2.06
36Ar/40Ar
39Ar/40Ar
Age (Ma)
Plateau Age (1σ): 12.22 ± 0.13 Ma
TF Age: 12.4 ± 0.13 Ma
%Ar cumulative
d
LA15 - Amphiboles
Isochron Age:
14.30 ± 0.33Ma
40Ar/36Ar: 352.6 ± 7.1
MSWD: 1.61
36Ar/40Ar
39Ar/40Ar
Age (Ma)
Plateau Age (1σ): 15.23 ± 0.26 Ma
TF Age: 19.20 ± 0.28 Ma
%Ar cumulative
e
LA33 - Muscovites
Isochron Age:
10.92 ± 0.21Ma
40Ar/36Ar: 333.55 ± 4.8
MSWD: 1.94
36Ar/40Ar
39Ar/40Ar
Age (Ma)
Plateau Age (1σ): 10.75 ± 0.14 Ma
TF Age: 12.4 ± 0.28 Ma
%Ar cumulative
f
LA47 - Muscovites
Isochron Age:
8.68 ± 0.33 Ma
40Ar/36Ar: 358.57 ± 8.2
MSWD: 6.43
36Ar/40Ar
39Ar/40Ar
g
LA58 - Muscovites
Isochron Age:
9.92± 0.24 Ma
40Ar/36Ar: 325.2 ± 3.6
MSWD: 1.68
36Ar/40Ar
39Ar/40Ar
h
LA13 - Muscovites
Isochron Age:
8.86 ± 0.36Ma
40Ar/36Ar: 329.0 ± 6.1
MSWD: 4.51
36Ar/40Ar
39Ar/40Ar
Age (Ma)
Plateau Age (1σ):
10.71 ± 0.19 Ma
TF Age: 9.16 ± 0.11 Ma
%Ar cumulative
i
LA14 - Muscovites
Isochron Age:
6.8 ± 0.2 Ma
40Ar/36Ar: 305.6 ± 5.0
MSWD: 1.43
36Ar/40Ar
39Ar/40Ar
Age (Ma)
Plateau Age (1σ):
7.1 ± 0.1 Ma
TF Age: 11.4 ± 0.08 Ma
%Ar cumulative
j
LA18 - Muscovites
Isochron Age:
9.7 ± 0.2 Ma
40Ar/36Ar: 320.9 ± 3.4
MSWD: 4.61
36Ar/40Ar
39Ar/40Ar
k
LA14 - biotites
Isochron Age:
8.86 ± 0.13 Ma
40Ar/36Ar: 304.2 ± 3.7
MSWD: 2.1
36Ar/40Ar
39Ar/40Ar
Age (Ma)
Plateau Age (1σ): 8.79 ± 0.11 Ma
TF Age: 9.30 ± 0.11 Ma
%Ar cumulative
l
LA18 - biotites
Isochron Age:
8.94 ± 0.14 Ma
40Ar/36Ar: 323.6 ± 5.2
MSWD: 3.09
36Ar/40Ar
39Ar/40Ar

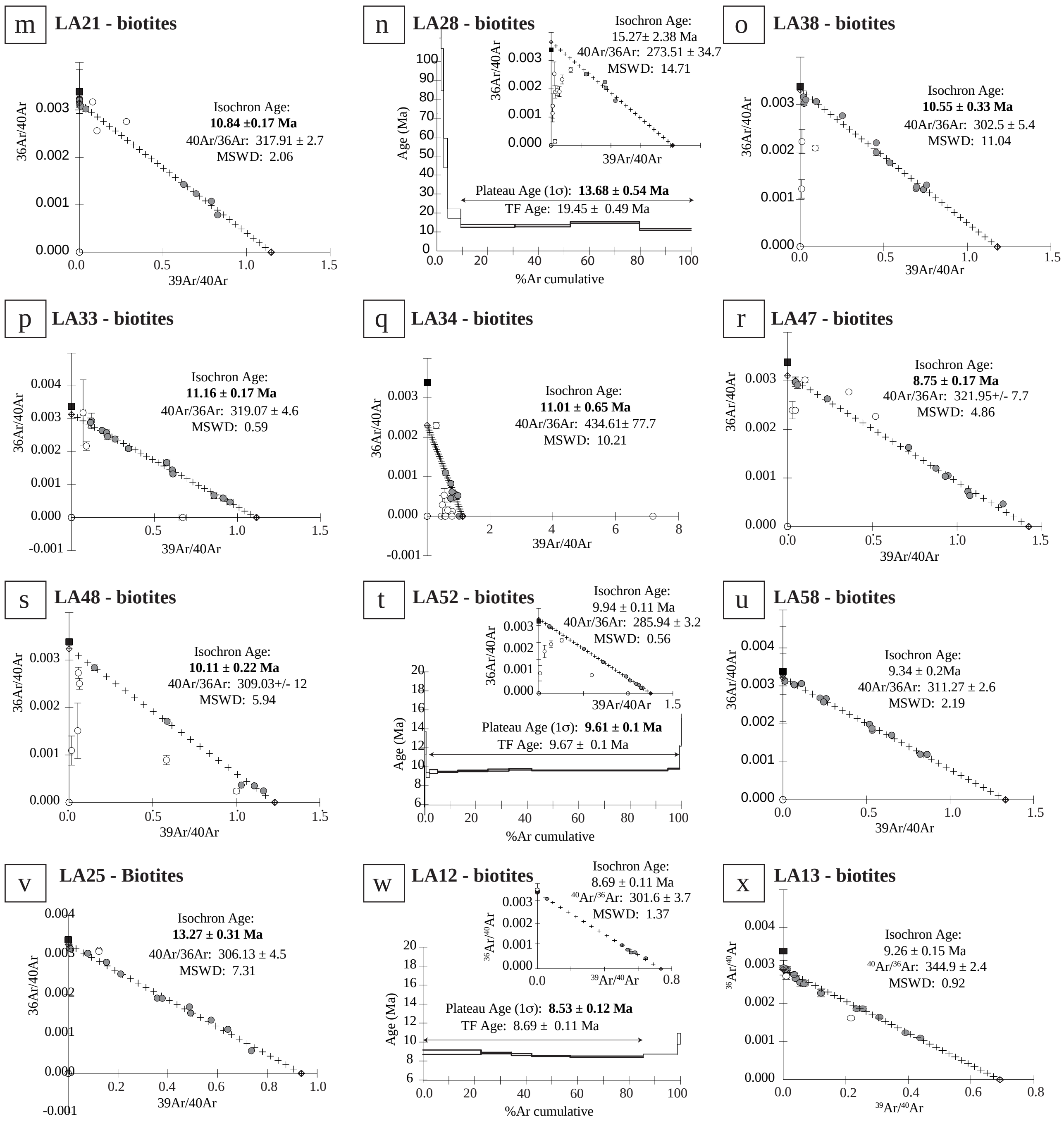

m
LA21 - biotites
Isochron Age:
10.84 ±0.17 Ma
40Ar/36Ar: 317.91 ± 2.7
MSWD: 2.06
36Ar/40Ar
39Ar/40Ar
n
LA28 - biotites
Isochron Age:
15.27± 2.38 Ma
40Ar/36Ar: 273.51 ± 34.7
MSWD: 14.71
Plateau Age (1σ): 13.68 ± 0.54 Ma
TF Age: 19.45 ± 0.49 Ma
Age (Ma)
%Ar cumulative
o
LA38 - biotites
Isochron Age:
10.55 ± 0.33 Ma
40Ar/36Ar: 302.5 ± 5.4
MSWD: 11.04
p
LA33 - biotites
Isochron Age:
11.16 ± 0.17 Ma
40Ar/36Ar: 319.07 ± 4.6
MSWD: 0.59
q
LA34 - biotites
Isochron Age:
11.01 ± 0.65 Ma
40Ar/36Ar: 434.61± 77.7
MSWD: 10.21
r
LA47 - biotites
Isochron Age:
8.75 ± 0.17 Ma
40Ar/36Ar: 321.95+/- 7.7
MSWD: 4.86
s
LA48 - biotites
Isochron Age:
10.11 ± 0.22 Ma
40Ar/36Ar: 309.03+/- 12
MSWD: 5.94
t
LA52 - biotites
Isochron Age:
9.94 ± 0.11 Ma
40Ar/36Ar: 285.94 ± 3.2
MSWD: 0.56
Plateau Age (1σ): 9.61 ± 0.1 Ma
TF Age: 9.67 ± 0.1 Ma
u
LA58 - biotites
Isochron Age:
9.34 ± 0.2Ma
40Ar/36Ar: 311.27 ± 2.6
MSWD: 2.19
v
LA25 - Biotites
Isochron Age:
13.27 ± 0.31 Ma
40Ar/36Ar: 306.13 ± 4.5
MSWD: 7.31
w
LA12 - biotites
Isochron Age:
8.69 ± 0.11 Ma
40Ar/36Ar: 301.6 ± 3.7
MSWD: 1.37
Plateau Age (1σ): 8.53 ± 0.12 Ma
TF Age: 8.69 ± 0.11 Ma
x
LA13 - biotites
Isochron Age:
9.26 ± 0.15 Ma
40Ar/36Ar: 344.9 ± 2.4
MSWD: 0.92

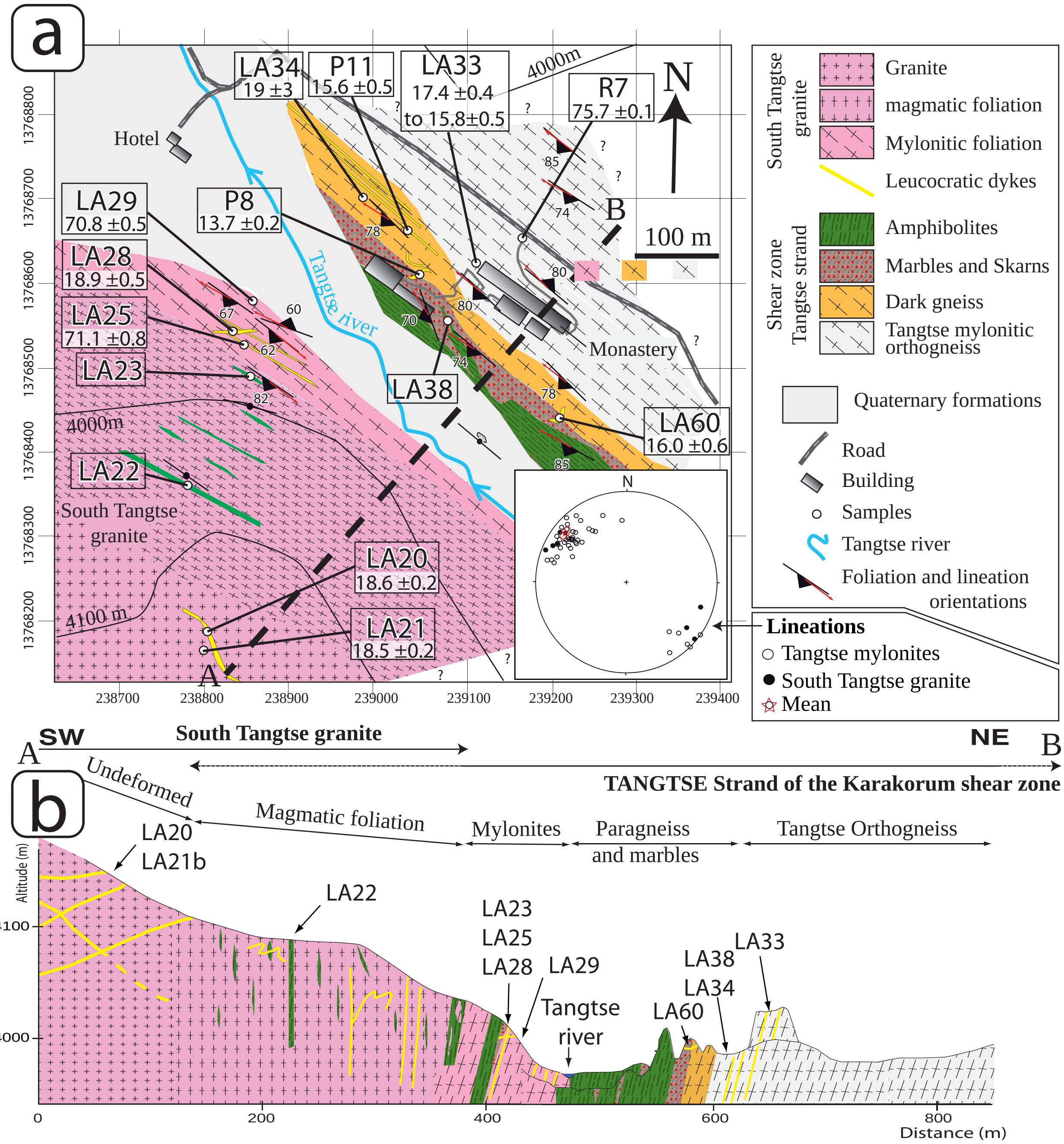

a
LA34
19 ±3
P11
15.6 ±0.5
LA33
17.4 ±0.4
to 15.8±0.5
4000m
R7
75.7 ±0.1
N
Hotel
LA29
70.8 ±0.5
P8
13.7 ±0.2
LA28
18.9 ±0.5
LA25
71.1 ±0.8
LA23
LA38
Tangtse river
Monastery
B
100 m
4000m
LA60
16.0 ±0.6
LA22
South Tangtse
granite
LA20
18.6 ±0.2
4100 m
LA21
18.5 ±0.2
A
13768800
13768700
13768600
13768500
13768400
13768300
13768200
238700
238800
238900
239000
239100
239200
239300
239400
South Tangtse granite
Granite
magmatic foliation
Mylonitic foliation
Leucocratic dykes
Shear zone Tangtse strand
Amphibolites
Marbles and Skarns
Dark gneiss
Tangtse mylonitic orthogneiss
Quaternary formations
Road
Building
Samples
Tangtse river
Foliation and lineation orientations
Lineations
Tangtse mylonites
South Tangtse granite
Mean
A SW
South Tangtse granite
NE B
TANGTSE Strand of the Karakorum shear zone
b
Undeformed
Magmatic foliation
Mylonites
Paragneiss and marbles
Tangtse Orthogneiss
LA20
LA21b
LA22
LA23
LA25
LA28
LA29
Tangtse river
LA38
LA34
LA60
LA33
Altitude (m)
4100
4000
0
200
400
600
800
Distance (m)

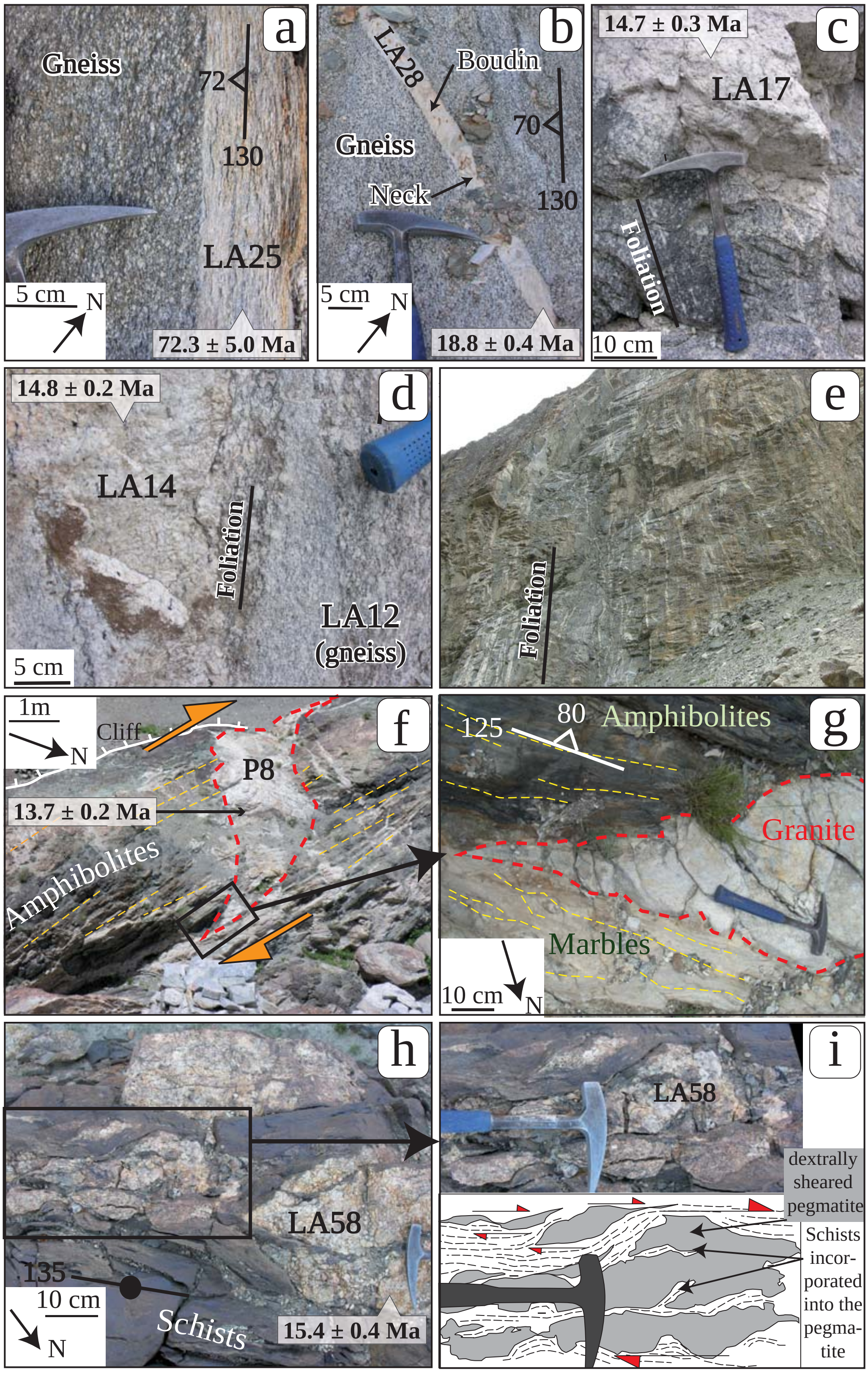

a
Gneiss
72
130
LA25
5 cm
N
72.3 ± 5.0 Ma
b
LA28
Boudin
70
130
Gneiss
Neck
5 cm
N
18.8 ± 0.4 Ma
c
14.7 ± 0.3 Ma
LA17
Foliation
10 cm
d
14.8 ± 0.2 Ma
LA14
Foliation
LA12
(gneiss)
5 cm
e
Foliation
f
1m
Cliff
N
P8
13.7 ± 0.2 Ma
Amphibolites
g
125
80
Amphibolites
Granite
Marbles
10 cm
N
h
LA58
135
10 cm
N
Schists
15.4 ± 0.4 Ma
i
LA58
dextrally sheared pegmatite
Schists incor-porated into the pegma-tite

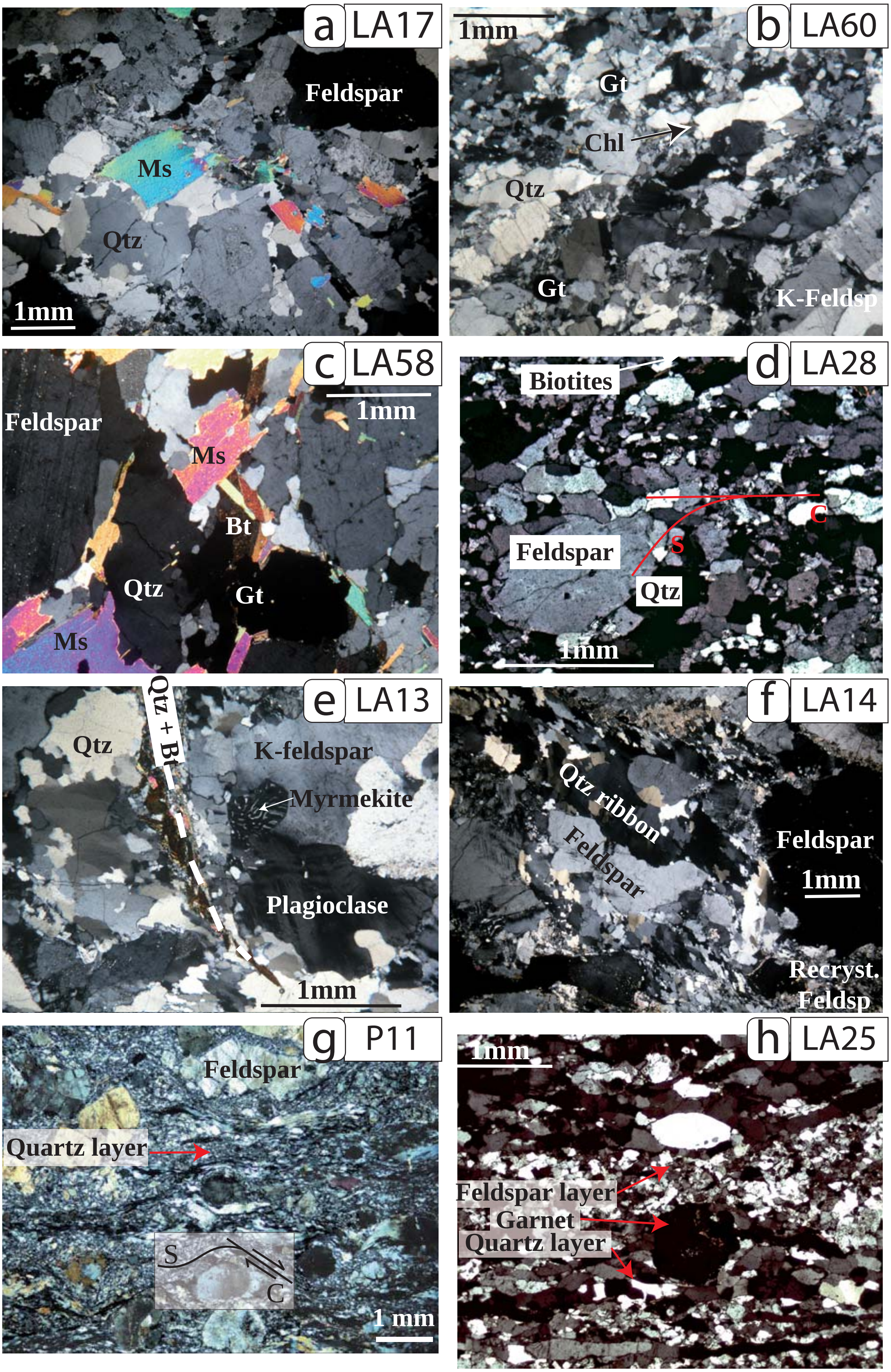
a
LA17
Feldspar
Ms
Qtz
1mm
b
LA60
1mm
Gt
Chl
Qtz
Gt
K-Feldsp
c
LA58
1mm
Feldspar
Ms
Bt
Qtz
Gt
Ms
d
LA28
Biotites
C
S
Feldspar
Qtz
1mm
e
LA13
Qtz + Bt
Qtz
K-feldspar
Myrmekite
Plagioclase
1mm
f
LA14
Qtz ribbon
Feldspar
Feldspar
1mm
Recryst.
Feldsp
g
P11
Feldspar
Quartz layer
S
C
1 mm
h
LA25
1mm
Feldspar layer
Garnet
Quartz layer

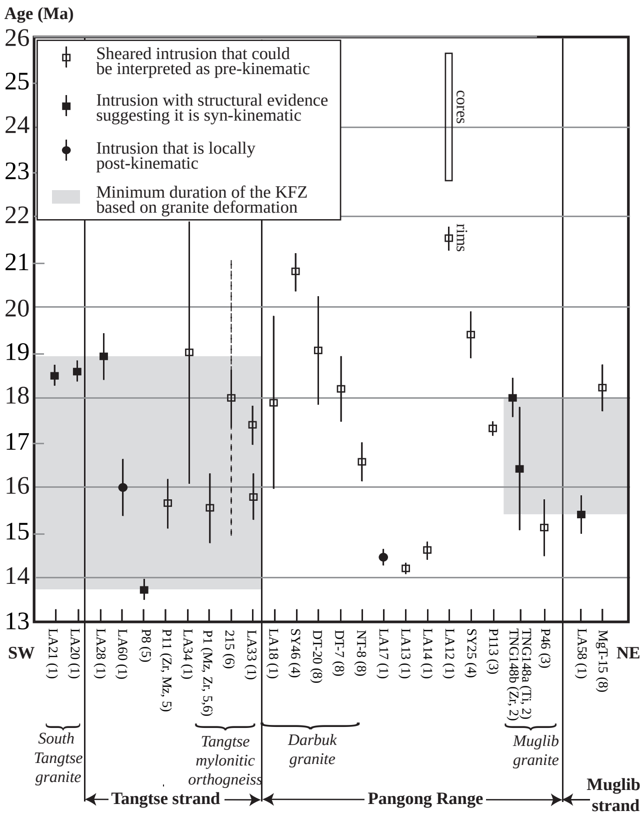

Age (Ma)
26
25
24
23
22
21
20
19
18
17
16
15
14
13
Sheared intrusion that could be interpreted as pre-kinematic
Intrusion with structural evidence suggesting it is syn-kinematic
Intrusion that is locally post-kinematic
Minimum duration of the KFZ based on granite deformation
cores
rims
SW
LA21 (1)
LA20 (1)
LA28 (1)
LA60 (1)
P8 (5)
P11 (Zr, Mz, 5)
LA34 (1)
P1 (Mz, Zr, 5,6)
215 (6)
LA33 (1)
LA18 (1)
SY46 (4)
DT-20 (8)
DT-7 (8)
NT-8 (8)
LA17 (1)
LA13 (1)
LA14 (1)
LA12 (1)
SY25 (4)
P113 (3)
TNG148a (Ti, 2)
TNG148b (Zr, 2)
P46 (3)
LA58 (1)
MgT-15 (8)
NE
South Tangtse granite
Tangtse mylonitic orthogneiss
Darbuk granite
Muglib granite
Tangtse strand
Pangong Range
Muglib strand

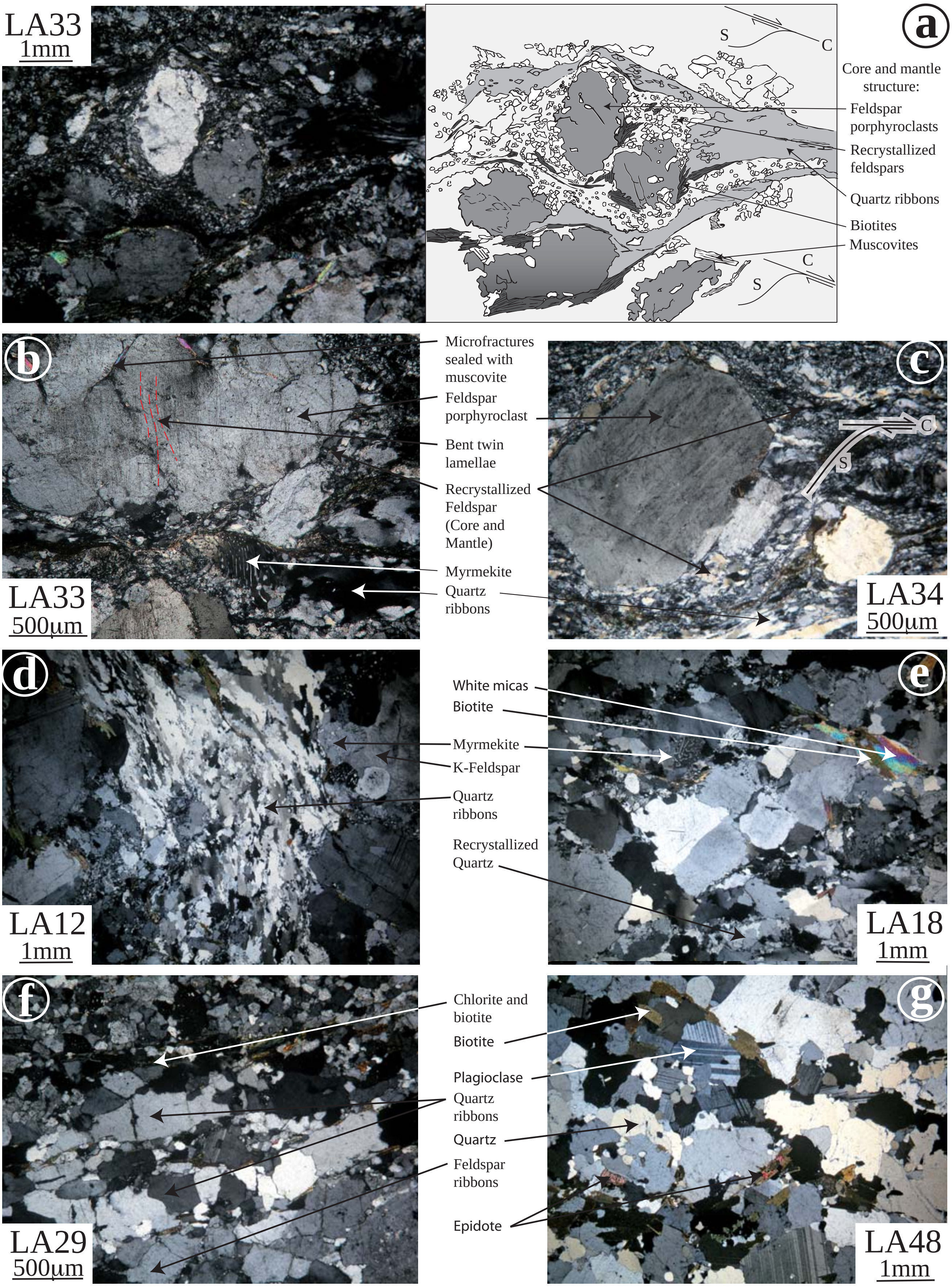
LA33
1mm
a
S
C
Core and mantle structure:
Feldspar porphyroclasts
Recrystallized feldspars
Quartz ribbons
Biotites
Muscovites
C
S
b
Microfractures sealed with muscovite
Feldspar porphyroclast
Bent twin lamellae
Recrystallized Feldspar (Core and Mantle)
Myrmekite
Quartz ribbons
LA33
500µm
c
C
S
LA34
500µm
d
LA12
1mm
White micas
Biotite
Myrmekite
K-Feldspar
Quartz ribbons
Recrystallized Quartz
e
LA18
1mm
f
Chlorite and biotite
Biotite
Plagioclase
Quartz ribbons
Quartz
Feldspar ribbons
Epidote
g
LA29
500µm
LA48
1mm

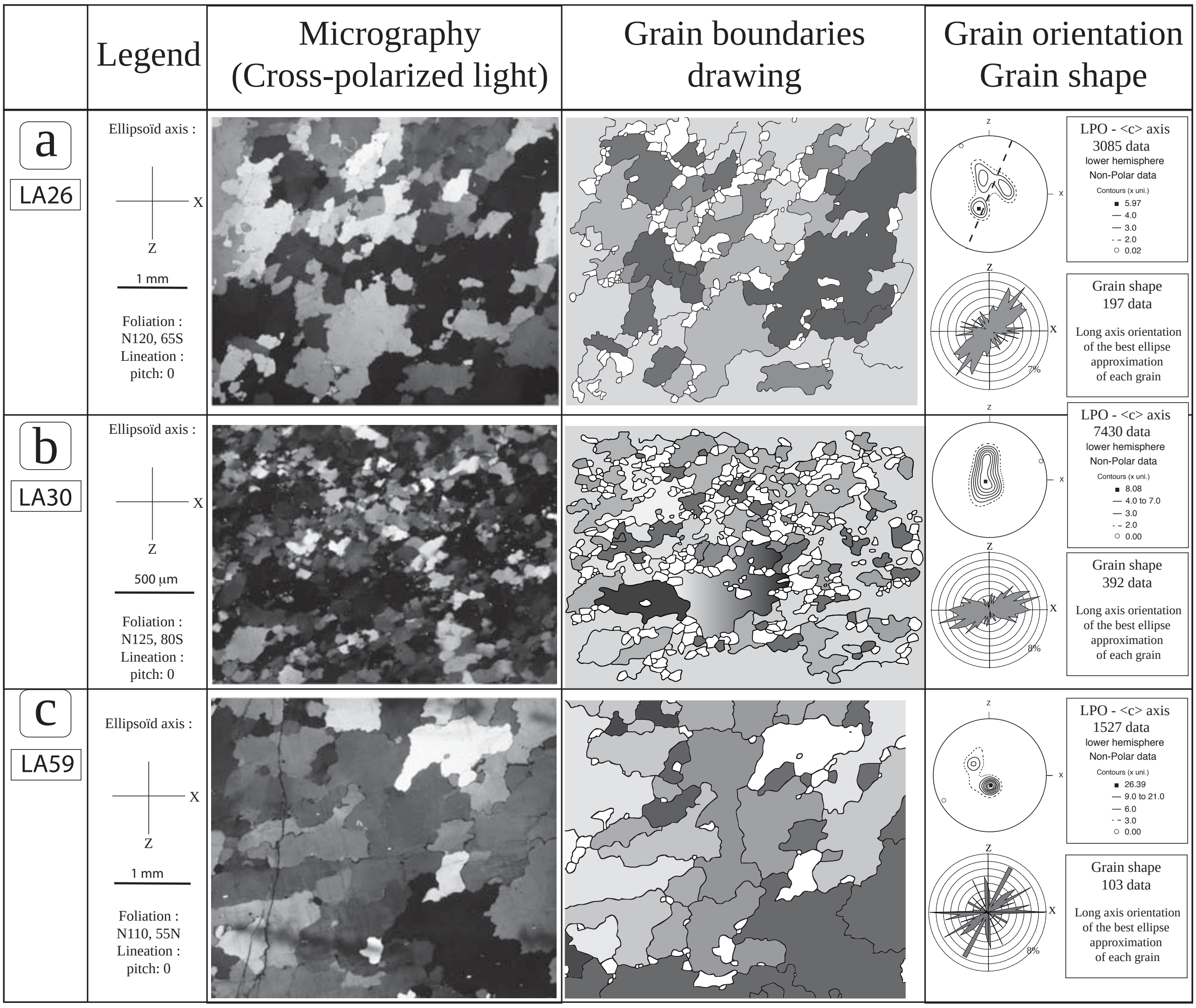

Legend
Micrography (Cross-polarized light)
Grain boundaries drawing
Grain orientation Grain shape
a
LA26
Ellipsoïd axis :
X
Z
1 mm
Foliation : N120, 65S
Lineation : pitch: 0
LPO - <c> axis
3085 data
lower hemisphere
Non-Polar data
Contours (x uni.)
5.97
4.0
3.0
2.0
0.02
Grain shape
197 data
Long axis orientation of the best ellipse approximation of each grain
7%
b
LA30
Ellipsoïd axis :
X
Z
500 µm
Foliation : N125, 80S
Lineation : pitch: 0
LPO - <c> axis
7430 data
lower hemisphere
Non-Polar data
Contours (x uni.)
8.08
4.0 to 7.0
3.0
2.0
0.00
Grain shape
392 data
Long axis orientation of the best ellipse approximation of each grain
8%
c
LA59
Ellipsoïd axis :
X
Z
1 mm
Foliation : N110, 55N
Lineation : pitch: 0
LPO - <c> axis
1527 data
lower hemisphere
Non-Polar data
Contours (x uni.)
26.39
9.0 to 21.0
6.0
3.0
0.00
Grain shape
103 data
Long axis orientation of the best ellipse approximation of each grain
8%

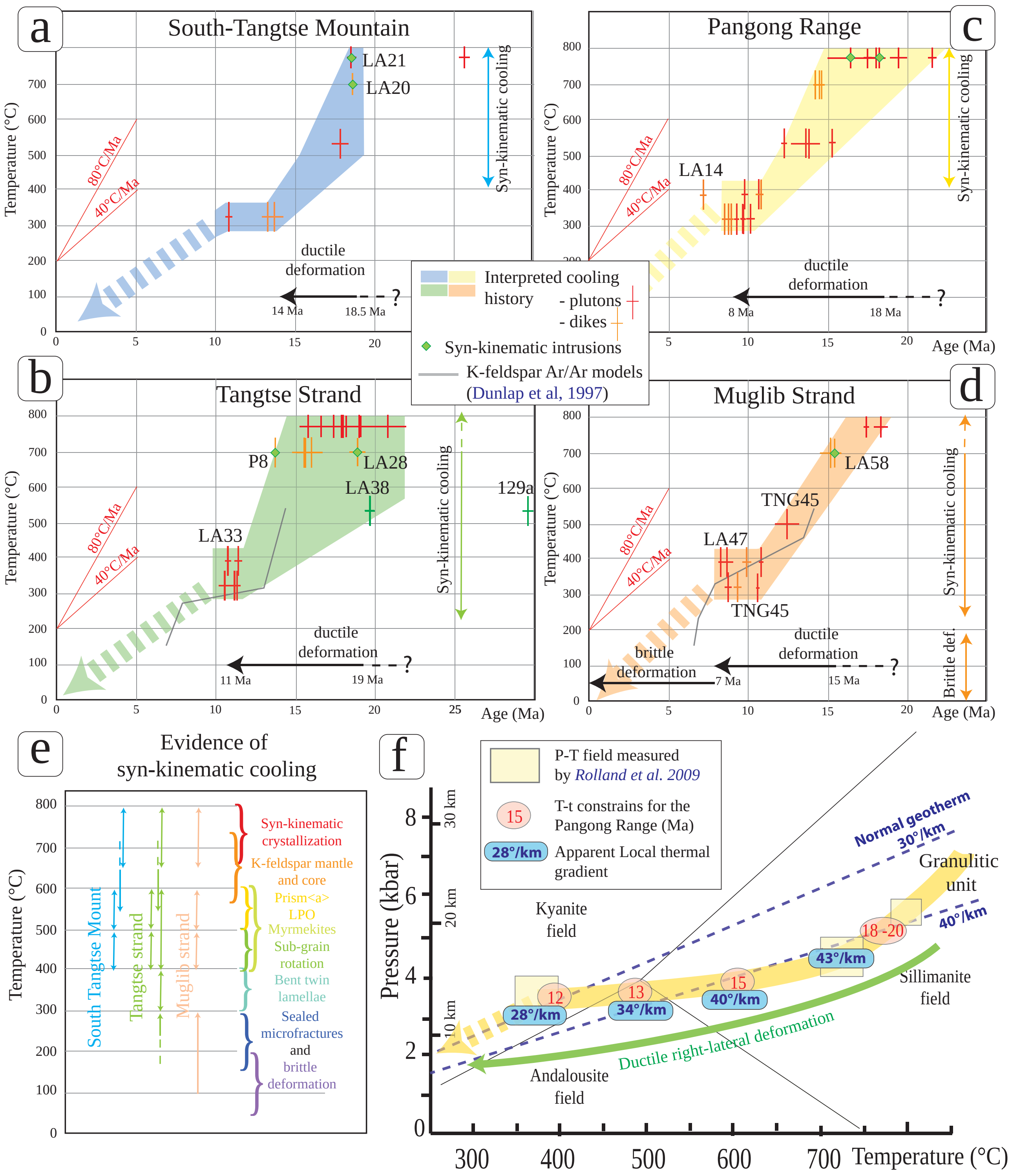
a
South-Tangtse Mountain
LA21
LA20
Syn-kinematic cooling
80°C/Ma
40°C/Ma
ductile
deformation
14 Ma
18.5 Ma
Temperature (°C)
b
Tangtse Strand
P8
LA28
LA38
129a
LA33
Syn-kinematic cooling
ductile
deformation
11 Ma
19 Ma
Age (Ma)
c
Pangong Range
LA14
Syn-kinematic cooling
ductile
deformation
8 Ma
18 Ma
d
Muglib Strand
LA58
TNG45
LA47
TNG45
brittle
deformation
7 Ma
15 Ma
Brittle def.
Interpreted cooling history
- plutons
- dikes
Syn-kinematic intrusions
K-feldspar Ar/Ar models
(Dunlap et al, 1997)
e
Evidence of
syn-kinematic cooling
South Tangtse Mount
Tangtse strand
Muglib strand
Syn-kinematic crystallization
K-feldspar mantle and core
Prism<a> LPO
Myrmekites
Sub-grain rotation
Bent twin lamellae
Sealed microfractures
and
brittle deformation
f
P-T field measured by Rolland et al. 2009
T-t constrains for the Pangong Range (Ma)
28°/km Apparent Local thermal gradient
Pressure (kbar)
30 km
20 km
10 km
Kyanite field
Normal geotherm 30°/km
Granulitic unit
40°/km
43°/km
18 -20
Sillimanite field
12
13
15
28°/km
34°/km
40°/km
Ductile right-lateral deformation
Andalousite field
Temperature (°C)

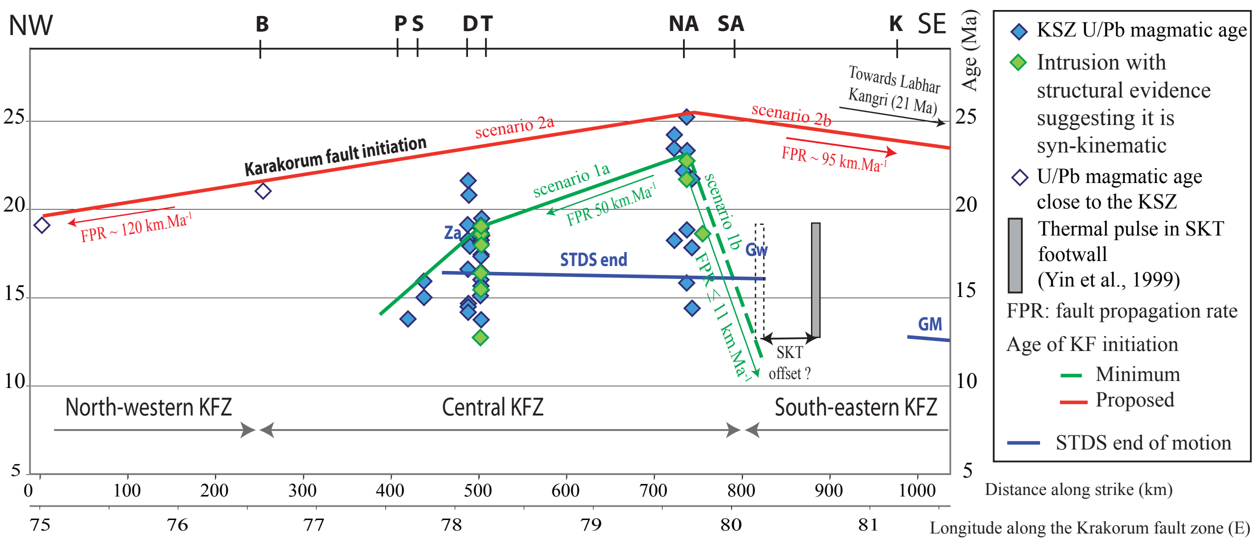

NW
B
P S
D T
NA
SA
K
SE
Age (Ma)
Towards Labhar Kangri (21 Ma)
scenario 2a
scenario 2b
Karakorum fault initiation
FPR ~ 95 km.Ma-1
scenario 1a
FPR 50 km.Ma-1
scenario 1b
FPR ≤ 11 km.Ma-1
FPR ~ 120 km.Ma-1
Za
STDS end
Gw
GM
SKT offset ?
North-western KFZ
Central KFZ
South-eastern KFZ
Distance along strike (km)
Longitude along the Krakorum fault zone (E)
KSZ U/Pb magmatic age
Intrusion with structural evidence suggesting it is syn-kinematic
U/Pb magmatic age close to the KSZ
Thermal pulse in SKT footwall (Yin et al., 1999)
FPR: fault propagation rate
Age of KF initiation
Minimum
Proposed
STDS end of motion

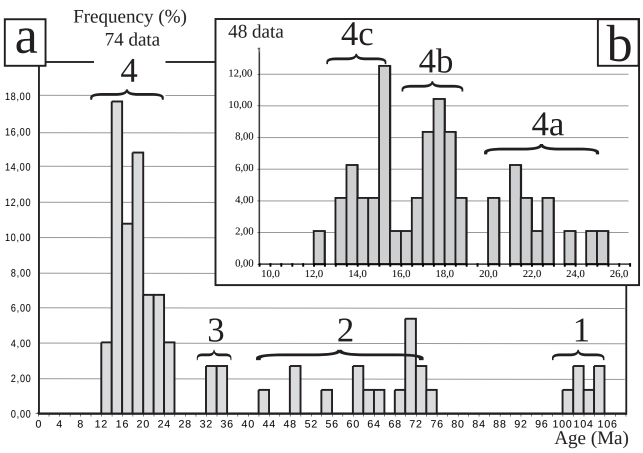

a
Frequency (%)
74 data
4
3
2
1
Age (Ma)
b
48 data
4c
4b
4a

Table 1: Sample characteristics and location

Site		Samples						Mineral dated			Temperature of deformation	
Section	zone	Name	Location (lat/long, WGS84)		Facies	Deformation	Relation with deformation	U/Pb mineral	U/Pb method	Ar/Ar	Quartz-Feldspar relationships	Quartz microstructures and fabrics
			lat	long							(°C)	(°C)
Darbuk section	Pangong Range	LA12	78.112972	34.146694	orthogneiss	strongly deformed	pre or syn-kinematic	Zircons	La-ICP-MS	Bt	> 550 ±50 to < 300	
Darbuk section	Pangong Range	LA13	78.112972	34.146694	pegmatite	slightly deformed	pre or syn-kinematic	Zircons	La-ICP-MS	Bt, Mu	450 ±50 to < 300	
Darbuk section	Pangong Range	LA14	78.112972	34.146694	leucocratic dike	slightly deformed	pre or syn-kinematic	Zircons	La-ICP-MS	Bt, Mu	450 ±50 to < 300	
Darbuk section	Pangong Range	LA15	78.112972	34.146694	amphibolite	strongly deformed	pre or syn-kinematic			Amph		
Darbuk section	Pangong Range	LA17	78.106388	34.143666	pegmatite	undeformed cross-cutting foliation	locally post-kinematic	Zircons	La-ICP-MS			
Darbuk section	Pangong Range	LA18	78.108	34.126333	2-micas granite	strongly deformed	pre or syn-kinematic	Zircons	La-ICP-MS	Bt, Mu	450 ±50 to < 300	
Tangtse section	South Tangtse mountain	LA20*	78.171444	34.021611	leucocratic dyke	undeformed	syn-kinematic	Zircons	SHRIMP*			
Tangtse section	South Tangtse mountain	LA21b*	78.171444	34.021611	leucogranite	undeformed	syn-kinematic	Zircons	SHRIMP*	Bt		
Tangtse section	South Tangtse mountain	LA23	78.171833	34.025027	amphibolite	strongly deformed	pre or syn-kinematic			Amph		
Tangtse section	South Tangtse mountain	LA25	78.171833	34.025027	leucocratic dike	strongly deformed	pre or syn-kinematic	Zircons	SHRIMP	Bt	> 550 ±50	
Tangtse section	South Tangtse mountain	LA26	78.171833	34.025027	quartz ribbon	strongly deformed	pre or syn-kinematic					550 ±50 to 450 ±50
Tangtse section	South Tangtse mountain	LA28	78.171833	34.025027	leucocratic dike	deformed cross-cutting foliation	syn-kinematic	Zircons	SHRIMP	Bt	> 550 ±50	
Tangtse section	South Tangtse mountain	LA29	78.171944	34.025305	orthogneiss	strongly deformed	pre or syn-kinematic	Zircons	La-ICP-MS		> 550 ±50	
Tangtse section	Tangtse strand	LA30	78.025916	34.17375	quartz ribbon	strongly deformed	pre or syn-kinematic					450 ±50
Tangtse section	Tangtse strand	LA33	78.174666	34.025777	leucocratic gneiss	strongly deformed	pre or syn-kinematic	Zircons	La-ICP-MS	Bt, Mu	> 550 ±50 to < 300	
Tangtse section	Tangtse strand	LA34	78.173138	34.026555	dark gneiss	strongly deformed	pre or syn-kinematic	Zircons	La-ICP-MS	Bt	> 650 to < 300	
Tangtse section	Tangtse strand	LA38	78.025916	34.17375	amphibolite	strongly deformed	pre or syn-kinematic			Amph, Bt		
Muglib strand	Muglib strand	LA47	78.303111	34.009138	schist	strongly deformed	pre or syn-kinematic			Bt, Mu		
Tangtse section	Pangong Range	LA48	78.211055	34.035638	leucogranite	slightly deformed	pre or syn-kinematic	Zircons	La-ICP-MS	Bt		
Tangtse section	Pangong Range	LA52	78.221027	34.039888	granodiorite	strongly deformed	pre or syn-kinematic			Bt, Amph		
Tangtse section	Muglib strand	LA58	78.245888	34.052861	leucocratic dike	slightly deformed	pre or syn-kinematic	Zircons	SHRIMP	Bt, Mu	> 550 ±50 to 450 ±50	
Tangtse section	Muglib strand	LA59	78.245888	34.052861	quartz ribbon	slightly deformed	pre or syn-kinematic					550 ±50
Tangtse section	Tangtse strand	LA60*	78.175666	34.024222	leucocratic dike	undeformed cross-cutting foliation	locally post-kinematic	Zircons	SHRIMP*			

Felds: Feldspar ; Bt: Biotite ; Amph: Amphiboles ; Mu: Muscovite
*: Leloup et al., 2011

Table 2: U/Pb ages

Sample				Spot conditions	Average 206Pb/238U age				207Pb/206Pb vs 238U/206Pb (Terra-Wesserberg) age					interpretation	
Name	Rock type	Characteristics	mineral type		Age (Ma)	MSWD	Number of spots/ grains	Spots (crystal n°/ border (b) or core (c))	Lower intercept (Ma)	Upper intercept (Ma)	MSWD	Number of spots/ grains	Spots (crystal n°/ border (b) or core (c))	Th/U (mean)	interpretation
LA12	Gneiss	dextrally sheared	zircon	26 µm 4mJ 4Hz	**21.5 ± 0.2**	1.4	11/11	*1c. 2c. 5b. 9b. 14b. 16b. 20b. 25b. 27b. 32b. 28b*	21.9 ± 0.3	-	1.2	11/11	*1c. 2c. 5b. 9b. 14b. 16b. 20b. 25b. 27b. 32b. 28b*	0.40	crystallization age
					25.6 to 22.8	-	10/9	*3c. 6b. 7b. 11c. 14c. 29b. 32c. 29c. 21b. 15b*	-	-	-	-	-	0.38	inherited age or early crystallization age
LA13	Pegmatite	slightly deformed	zircon	11 µm 4mJ 3Hz	**14.2 ± 0.1**	1.1	9/4	*1b (*5). 3b (*2). 9b. 10b*	14.2 ± 0.1	-	1.9	9/4	*1b (*5). 3b (*2). 9b. 10b*	0.60	crystallization age
LA14	Leucocratic dike	slightly deformed	zircon	33 µm 4mJ 4Hz	14.6 ± 0.2	2.7	15/9	*2b. 3b (*2). 4b (*2). 6b (*2). 9b (*2). 12b. 13b (*2). 15b (*2). 16b*	**14.8 ± 0.2**	-	2.0	15/9	*2b. 3b (*2). 4b (*2). 6b (*2). 9b (*2). 12b. 13b (*2). 15b (*2). 16b*	0.14	crystallization age
					65.0 to 29.9	-	2/2	*1c. 7c*	-	-	-	-	-	0.43	inherited age
LA17	Pegmatite	cross- cutting	zircon	20 µm 4mJ 4Hz	14.5 ± 0.2	1.9	12/10	*1b. 2c. 3b. 7b (*2). 8b. 9b (*3). 10b. 13b (*2)*	**14.7 ± 0.3**	-	0.9	12/10	*1b. 2c. 3b. 7b (*2). 8b. 9b (*3). 10b. 13b (*2)*	0.04	crystallization age
					64.2 to 24.4	-	4/3	*6c. 7c. 11c (*2)*	-	-	-	-	-	0.36	inherited age
LA18	Mylonite	dextrally sheared	zircon	33 µm 4mJ 4Hz	**17.9 ± 1.9**	9.9	3/3	*1b, 2b, 5b*	17.0 ± 3.0	-	9.9	4/4	*1b, 2b, 5b, 4b*	0.08	crystallization age
LA20**	leucocratic dyke	undeformed	zircon	Session 2 - 1&2	**18.6 ± 0.2**	2.2	10/10	*1b. 2b. 5b. 10b. 11b. 14b. 18b. 19b. 20b. 21b*	18.6 ± 0.3	5139 ± 150	1.8	17/14	*all except: 7b. 9b. 15b. 17b. 21b*	0.34	crystallization age
				Session 1	25.6 ± 0.3	-	1/1	*17c*	-	-	-	-	-	0.06	inherited age
LA21b**	leucogranite	undeformed	zircon	Session 2 - 1&2	**18.5 ± 0.2**	2.07	11/11	*2b. 4b. 5b. 6b. 8b. 9b. 11b. 22b. 25b. 26b. 28b*	18.6 ± 0.2	5158 ± 170	1.8	19/19	*2b. 4b. 5b. 6b. 8b. 9b. 11b. 22b. 25b. 26b. 28b*	0.32	crystallization age
				Session 1	310 ± 5	-	1/1	*20c*	-	-	-	-	-	0.19	inherited age
LA25*	Leucocratic dike	concordant with S1	zircon	Session 1	71.1 ± 0.8	1.6	4/4	*1b. 2b. 7b. 6b*	**72.3 ± 5.0**	5081 ± 0 (CLA)	3.6	5/4	*1b. 2b. 7b. 6.1b. 6.3b*	0.90	inherited age
LA28*	Leucocratic dike	cross cutting & deformed	zircon	Session 1 & 2	18.9 ± 0.5	58	6/4	*3b. 4.1b. 4.2b. 6.1b. 6.2b. 7b*	**18.8 ± 0.4**	5081 ± 0 (CLA)	1.9	6/4	*3b. 4.1b. 4.2b. 6.1b. 6.2b. 7b*	0.30	crystallization age
					435 ± 5	-	1/1	*7c*	-	-	-	-	-	0.27	inherited age
LA29	Mylonite	dextrally deformed	zircon	33 µm 4mJ 4Hz	70.8 ± 0.5	1.2	20/17	*1b. 2c. 3b. 4b-c. 5b. 6b(*2). 7b-c. 8b. 11b-c. 13b. 14b. 15b. 16b. 18b. 19b*	**71.3 ± 0.6**	-	1.4	21/17	*1b. 2c. 3b. 4b-c. 5b. 6b(*2). 7b-c. 8b. 11b-c. 12b. 13b. 14b. 15b. 16b. 18b*	1.02	old crystallization age
LA33	Mylonite	dextrally deformed	zircon	33 µm 4mJ 4Hz	15.7 ± 0.1	5.9	6/6	*6b. 26b. 8b. 12c. 22b. 7b*	**15.8 ± 0.5**	-	-	6/6	*6b. 26b. 8b. 12c. 22b. 7b*	0.14	crystallization age
					16.9 ± 0.4	11.4	6/6	*10b. 22b. 14b.21b. 15b. 2b*	**17.4 ± 0.4**	-	-	6/6	*10b. 22b. 14b.21b. 15b. 2b*	0.16	onset of magmatism
					65.4 ± 1.7	-	1/1	*10c*	-	-	-	-	-	0.51	inherited age
LA34	Dark gneiss	dextrally deformed	zircon	33 µm 4mJ 4Hz	-	-	-	-	-	**19.0 ± 2.9 (CLR)**	2.0	10/9	*4b. 5c. 8b (*2). 11b. 13b. 17b. 18c. 3b. 12b*	0.82	crystallization age
					63.8 ± 1.6	-	1/1	*3c*	-	-	-	-	-	1.11	inherited age
LA48	leucogranite	slightly deformed	zircon	33 µm 4mJ 4Hz	-	-	-	-	**105.1 ± 1.1**	-	1.2	10/2	*2b (*4). 7b (*6)*	0.78	old crystallization age
Sample				**Spot conditions**	**Age vs U(ppm) age 207 Pb corrected**										
Number	**Rock type**	**Characteristics**	**mineral type**		**Intercept at 2000ppm (Ma)**	**MSWD**	**Number of spots/ grains**	**Spots (crystal n°/ border (b) or core (c))**						**Th/U (mean)**	**interpretation**
LA58*	Leucocratic dike	transposed	zircon	Session 1 & 2	**15.4 ± 0.4**	1.4	6/6	*1b. 4b. 9b. 10b. 11b. 24b*	-	-	-	-	-	0.03	crystallization age
LA60**	Leucocratic dike	cross cutting	zircon	Session 1	**16.0 ± 0.6**	2.6	6/6	*2b. 3b. 4b. 6b. 14b. 17b*	-	-	-	-	-	0.03	crystallization age

* sample analysed by SHRIMP
** sample analysed by SHRIMP by Leloup et al., 2011
CLA = commun lead anchored
CLR = commun lead regression
Uncertainties reported at 1s and are calculated by using SQUID 2.22.08.04.30, rev. 30 Apr 2008
Calibration standard 6266; U = 910 ppm; Age = 559 Ma; 206Pb/238U = 0.09059
3 sessions have been runned by Leloup et al., 2011 and this study
Session 1 -beam size 13x16um. Error in 206Pb/238U calibration 1.0% (included). Standard Error in Standard calibration was 0.30% (not included in above errors but required when comparing data from different mounts).
Session 2 -beam size 17x23um. Error in 206Pb/238U calibration 1.23% (included). Standard Error in Standard calibration was 0.39% (not included in above errors but required when comparing data from different mounts).
Session 3: spot conditions are diretcly written in the table.

Table 3a : biotite Ar/Ar ages

Rock Type	Sample		*Age/ Plateau age*			*Inverse Isochron Age*			Total fusion age
	Number	Mineral type	Type	Age, Ma	%Ar	Age, Ma	40Ar/ 36Ar	MSWD	
gneiss	**LA12**	Biotite	WPA	**8.53 ± 0.12**	87	8.69 ± 0.11	301.56 ± 3.7	1.37	8.69 ± 0.11
leucocratic dyke	**LA13**	Biotite				**9.26 ± 0.15**	344.92 ± 2.4	0.92	14.26 ± 0.35
pegmatite	**LA14**	Biotite	WPA	**8.79 ± 0.11**	80	8.86 ± 0.13	304.23 ± 3.7	2.10	9.30 ± 0.11
granite	**LA18**	Biotite				**8.94 ± 0.14**	323.6 ± 5.2	3.09	9.70 ± 0.10
granite	**LA21**	Biotite				**10.84 ± 0.17**	317.91 ± 2.7	2.06	11.69 ± 0.16
leucocratic dyke	**LA25**	Biotite				**13.27 ± 0.31**	306.13 ± 4.5	7.31	13 ± 0.13
leucocratic dyke	**LA28**	Biotite	WPA	**13.68 ± 0.54**	90	15.27 ± 2.38	273.51 ± 34.7	14.71	19.45 ± 0.49
gneiss	**LA33**	Biotite				**11.16 ± 0.17**	319.07 ± 4.6	0.59	12.12 ± 0.67
gneiss	**LA34**	Biotite				**11.01 ± 0.65**	434.61 ± 77.7	10.21	13.26 ± 0.18
amphibolite	**LA38**	Biotite				**10.55 ± 0.33**	302.5 ± 5.4	11.04	10.38 ± 0.11
schist	**LA47**	Biotite				**8.75 ± 0.17**	321.95 ± 7.7	4.86	8.58 ± 0.09
granite	**LA48**	Biotite				**10.11 ± 0.22**	309.03 ± 12	5.94	10.15 ± 0.11
granodiorite	**LA52**	Biotite	WPA	**9.61 ± 0.10**	98	9.94 ± 0.11	285.94 ± 3.2	0.56	9.67 ± 0.1
leucocratic dyke	**LA58**	Biotite				**9.34 ± 0.20**	311.27 ± 2.6	2.19	10.58 ± 7.4

Table 3b : muscovite Ar/Ar ages

Rock Type	Sample		*Age/ Plateau age*			*Inverse Isochron Age*			Total fusion age
	Number	Mineral type	Type	Age, Ma	%Ar	Age, Ma	40Ar/ 36Ar	MSWD	
leucocratic dyke	**LA13**	Muscovite	WPA	**10.71 ± 0.19**	45	8.86 ± 0.36	329.0 ± 6.1	4.51	9.16 ± 0.11
pegmatite	**LA14**	Muscovite	WPA	***7.10 ± 0.11***	50	6.81 ± 0.22	305.6 ± 5.0	1.43	11.41 ± 0.08
granite	**LA18**	Muscovite				**9.74 ± 0.18**	320.9 ± 3.4	4.61	10.04 ± 0.11
gneiss	**LA33**	Muscovite	WPA	***10.75 ± 0.14***	90	10.92 ± 0.21	333.6 ± 4.8	1.94	12.4 ± 0.28
schist	**LA47**	Muscovite				***8.68 ± 0.33***	358.6 ± 8.2	6.43	11.04 ± 0.39
leucocratic dyke	**LA58**	Muscovite				**9.92 ± 0.24**	325.2 ± 3.6	1.68	10.88 ± 1.99

Table 3c : amphibole Ar/Ar ages

Rock Type	Sample		*Age/ Plateau age*			*Inverse Isochron Age*			Total fusion age
	Number	Mineral type	Type	Age, Ma	%Ar	Age, Ma	40Ar/ 36Ar	MSWD	
amphibolite	**LA15**	Amphibole	WPA	**15.23 ± 0.26**	72	14.30 ± 0.33	352.63 ± 7.1	1.61	19.20 ± 0.28
amphibolite	**LA23**	Amphibole				**17.82 ± 0.48**	334.48 ± 5	3.34	23.23 ± 10.88
amphibolite	**LA38**	Amphibole	WPA	**19.68 ± 0.26**	90	17.38 ± 0.8	359.08 ± 8.6	3.67	26.05 ± 9.39
granodiorite	**LA52**	Amphibole	WPA	**12.22 ± 0.13**	95	12.44 ± 0.19	296.99 ± 3.7	2.06	12.40 ± 0.13

WPA: weighted plateau age

Italic : muscovite younger than biotite, indicating that they have been lately reequilibrated

Table 4: KFZ offsets, onset ages and corresponding fault rates

	Kinematic constraints (offset value [km])	References for offset	timing (duration [Ma])	References for timing	remark	Fault rate (cm.a^{-1})
North KFZ						
Suture zone offsets	435 - 565	*Valli et al., 2008*	20	*Valli et al., 2008; this study*	Infered age	2.17 - 2.82
Aghil formation offset	149- 167	*Robinson, 2009*	20	*Valli et al., 2008*	infered age	0.75 - 0.84
Aghil formation offset	149- 167	*Robinson, 2009*	14.7±1	*Robinson, 2009 from Phillips et al.,*		1.08 ±0.13
Central KFZ						
Suture zone offsets	200 - 240	*Ratschbacher et al., 1994; Valli et al., 2008*	22.7	*Valli et al., 2008*	minimum KF age in North Ayilari	0.97 - 1.06
Suture zone offsets	200 - 240	*Ratschbacher et al., 1994; Valli et al., 2008*	18.8	*This study*	minimum KF age at Tangtse	1.06 - 1.28
Suture zone offsets	200 - 240	*Ratschbacher et al., 1994; Valli et al., 2008*	23-25	*Valli et al., 2008, This study*	Oldest magmatic ages	0.8 - 1.04
Indus River offset	120	*Gaudemer et al., 1989*	14 ±2	*Valli et al., 2007*	Age of rapid exhumation of the Ayilari	0.75 - 1.00
Baltoro granite offset	120 - 150	*Searle et al., 1998*	15.5	*Phillips et al., 2004; this study*	Age of the Tangtse granite	0.77 - 0.97
Offset of Quaternary moraines				*Chevalier et al., 2005*		1.07 ±0.07
Offset of Quaternary moraines				*Brown et al. 2002*		0.4 ±0.1
Geodesy - GPS				*Banerjee and burgman, 2008*		1 ±0.4
Geodesy - GPS				*Jade et al., 2004*		0.34 ±0.5
Geodesy - InSaR				*Wright et al., 2004*		0.1 ±0.3
South KFZ						
Kailash thrust offset	60.5 - 71.5	*Murphy et al., 2000*	≤13	*Yin et al., 1999*		≥ 0.55